arXiv:astro-ph/0108013 v1   1 Aug 2001

GALAXY MASS AND LUMINOSITY SCALING LAWS DETERMINED BY WEAK GRAVITATIONAL LENSING

Timothy A. McKay[1], Erin Scott Sheldon[1], Judith Racusin[1], Philippe Fischer[2], Uros Seljak[3], Albert Stebbins[4], David Johnston[5], Joshua A. Frieman[4,5], Neta A. Bahcall[3], J. Brinkmann[6], István Csabai[7,8], Masataka Fukugita[9], G. S. Hennessy[10], Robert B. Hindsley[11], Željko Ivezić[3], D.Q. Lamb[5], Jon Loveday[12], Robert H. Lupton[3], Jeffrey A. Munn[13], R. C. Nichol[14], Jeffrey R. Pier[13], Donald G. York[5,15]

Submitted to Astrophysical Journal: Last Modified 13-June-2001. Version 1.5

ABSTRACT

We present new measurements of scaling laws relating the luminosity of galaxies to the amplitude and shape of their dark matter halos. Early imaging and spectroscopic data from the Sloan Digital Sky Survey are used to make weak lensing measurements of the surface mass density contrast $\Delta\Sigma_+$ around classes of lens objects. This surface mass density contrast as a function of radius is a measure of the galaxy-mass correlation function (GMCF). Because spectroscopic redshifts are available for all lens objects, the mass and distance scales are well constrained. The GMCF measured around $\sim$31,000 lenses is well fit by a power law of the form $\Delta\Sigma_+ = (2.5^{+0.7}_{-0.6})(R/1\mathrm{Mpc})^{-0.8\pm0.2}h\mathrm{M}_\odot\mathrm{pc}^{-2}$. We compare this GMCF to galaxy luminosity, type, and environment, and find that it varies strongly with all three. We quantify these variations by comparing the normalization of a fit to the inner 260 h^{-1} kpc (M_{260}) to the galaxy luminosity. While M_{260} is not strongly related to luminosity in bluest band (u'), there is a simple, linear relation between M_{260} and luminosity in redder bands (g', r', i', and z'). We test the universality of these mass-to-light scalings by independently measuring them for spiral and elliptical galaxies, and for galaxies in a variety of environments. We find remarkable consistency in these determinations in the red bands, especially i' and z'. This consistency across a wide range of systems suggests that the measured scaling represents an excellent cosmic average, and that the integrated star formation history of galaxies is strongly related to the dark matter environments in which they form. Future studies of galaxy mass and its relation to luminosity should concentrate on luminosities measured in red bands.

Subject headings: dark matter — galaxies: fundamental parameters — galaxies: halos — gravitational lensing — large-scale structure of the universe

1. INTRODUCTION

1.1. *The galaxy-mass correlation function*

The relationship between the luminous matter which we observe in the Universe and the dark matter which dominates its dynamical evolution is elusive. Models of hierarchical structure formation based on N-body simulations now provide a relatively complete picture of the formation, evolution, and clustering properties of dark matter halos. Unfortunately, experimental determination of structure relies on observations of luminous galaxies. The formation of luminous galaxies involves a variety of complex physical phenomena; gas physics, star formation, and the feedback mechanisms into the interstellar medium. These processes are currently too complex for a direct simulation. As a result, the relationship between luminous galaxies and the dark matter environment in which they form is poorly determined. This uncertainty seriously limits our ability to directly compare cosmological observations of galaxies to N-body simulations. Measurements which connect the mass distribution so carefully studied in N-body simulations to the luminous galaxies which we observe play a crucial role in understanding the formation of structure in the universe.

The connection between luminous galaxies and the dark

[1] University of Michigan, Department of Physics, 500 East University, Ann Arbor, MI 48109

[2] Deptartment of Astronomy, Univ. of Toronto, Toronto, ONT, M5S, 3H8, Canada

[3] Princeton University Observatory, Princeton, NJ 08544

[4] Fermi National Accelerator Laboratory, P.O. Box 500, Batavia, IL 60510

[5] The University of Chicago, Department of Astronomy and Astrophysics, 5640 S. Ellis Ave., Chicago, IL 60637

[6] Apache Point Observatory, P.O. Box 59, Sunspot, NM 88349-0059

[7] Department of Physics and Astronomy, The Johns Hopkins University, 3701 San Martin Drive, Baltimore, MD 21218

[8] Department of Physics of Complex Systems, Eötvös University, Pázmány Péter sétány 1

[9] University of Tokyo, Institute for Cosmic Ray Research, Kashiwa, 2778582, Japan

[10] U.S. Naval Observatory, 3450 Massachusetts Ave., NW, Washington, DC 20392-5420

[11] Remote Sensing Division, Code 7215, Naval Research Laboratory, 4555 Overlook Ave. SW, Washington, DC 20375

[12] Astronomy Centre, University of Sussex, Falmer, Brighton BN1 9QJ, United Kingdom

[13] U.S. Naval Observatory, Flagstaff Station, P.O. Box 1149, Flagstaff, AZ 86002-1149

[14] Dept. of Physics, Carnegie Mellon University, 5000 Forbes Ave., Pittsburgh, PA-15232

[15] The University of Chicago, Enrico Fermi Institute, 5640 S. Ellis Ave., Chicago, IL 60637

matter structures in which they reside has traditionally been approached by attempting to measure the masses of galaxies as discrete objects. As our understanding of the formation of cosmic structure has evolved, it has become clear that the dark halos containing galaxies are not discrete structures, clearly separated from one another. N-body simulations reveal instead a continuous matter field, with structure gradually accreting on all scales. Galaxies are expected to form in collapsed halos, which merge with each other into larger halos. These halos typically extend out to large radii without any apparent cut-off in the density profile. At each level one expects to find several galaxies inside the halo of a given mass, but some of these may be too faint to enter into the observational sample. In this picture the concept of 'the' mass of a galaxy may be poorly defined. While it is still possible to discuss, in an average sense, the mass profile of a galaxy, or to measure the mass within a fixed aperture, it may be inappropriate to speak of a galaxy's total mass.

A more appropriate way to describe the relationship between luminous matter and mass is through correlation measures. The full statistical relationship between galaxies and dark matter can be expressed as a Galaxy-Mass Correlation Function (GMCF). Given a set of points marking the locations of galaxies, a GMCF measures the extent to which mass is clustered around these points. A simple version of the GMCF would describe the average projected mass density interior to a radius R from a galaxy location. If there were no correlation between the locations of galaxies and mass, this GMCF would be flat. If galaxies were isolated point objects with discrete and equal masses, the GMCF would fall off as R^{-2}. If galaxies are embedded in isolated isothermal dark halos with equal mass, the GMCF will fall off as R^{-1}.

If the luminous properties of galaxies (luminosity, morphology, stellar population, etc.) are affected by the dark matter environment in which they form, we expect this GMCF to vary as we select different classes of galaxies. In this sense, crucial information about the connection between luminous and dark matter is encoded in the scaling laws describing changes in the amplitude and shape of the GMCF with galaxy properties.

In this work we measure something closely related to the naive GMCF using weak gravitational lensing; the projected surface mass density contrast. It is the difference between the surface density interior to a projected radius R and the surface density at the radius R. This surface mass density contrast function is what we refer to in this paper as the galaxy-mass correlation function (GMCF). We will measure the way in which the amplitude and shape of this GMCF scales with lens luminosity, morphology, and local environment to better understand how luminous and dark matter in the universe are related. These measurements will be made in all five SDSS colors, allowing us to probe the relationship between global galaxy properties and various stellar populations.

A traditional way of expressing the relations between mass and light is to compare an aperture mass and luminosity in a region studied. This mass-to-light ratio M/L, measured in solar units $M_{\odot}/L_{\odot}$, provides a convenient expression of the relative importance of dark and luminous matter in the region studied. It can be dependent on wavelength, and hence is usually denoted by an observed passband; for example $M/L_{g'}$ is the mass-to-light ratio, in solar units, measured in the SDSS g' band. When we speak of a mass-to-light ratio we implicitly assume a linear relationship between mass and light. In general we expect M/L to be a function, which may depend on scale, luminosity, galaxy type, and environment.

1.2. Methods of measuring galaxy masses

The quantity and distribution of mass in the universe has usually been determined by dynamical means. Motions of luminous test bodies are used to constrain mass distributions. Test masses are, of course, primarily sensitive to mass interior to the radius of their orbits. Within galaxies, the motions of stars and gas give strong evidence for dark components of disks and for extremely massive, extended halos of dark matter (Sackett 1995). On halo scales satellite galaxies can be used to probe the matter distribution. Studies of satellites give strong, but model dependent, suggestions that dark matter halos extend far beyond the luminous cores of galaxies (Zaritsky et al. 1997; Zaritsky 1999), merging smoothly into the halos of their neighbors.

On larger scales, the presence of mass can be inferred from the motions of galaxies in groups (Girardi & Giuricin 2000), clusters (Carlberg, Yee, & Ellingson 1997), and beyond (Willick 2000). In relaxed groups and clusters mass is also revealed by the emission of thermal x-rays from a hot intergalactic medium. This x-ray emission can be used to place strong constraints on group and cluster masses on these large scales (Evrard, Metzler, & Navarro 1996; Hradecky et al. 2000).

Dynamical measures of mass are extremely powerful. They have revealed the dominant role of dark matter in the universe, and given us important hints about its distribution. They have shown (Bahcall, et al. 2000) that M/L, measured around galaxy centers, increases smoothly from small ($10\ h^{-1}$ kpc) to large ($250\ h^{-1}$ kpc) scales. At larger scales M/L is more or less constant. This increase with scale is not surprising, it reflects how baryonic material cools and collapses to the center of dark matter halos. The baryons collapse into a rotationally supported disk, with its scale determined by the angular momentum of baryons. Assuming the angular momentum is not transferred from dark matter to baryons and that its initial value is appropriate for CDM models one finds the disk scale length at least a factor of 10 smaller than the extent of the dark matter halo. As a result, most of the light is found in the centers of dark matter potential wells, while most of the mass remains in an extended halo.

A limitation of the dynamical approach is that it requires the presence of luminous tracers. In addition, the motions of test particles are very little affected by the presence of matter outside the radius of their orbits. As a result, dynamical measures have primarily measured the mass of the inner parts ($<30\ h^{-1}$ kpc) of galaxy halos. Naive comparison of dynamical masses measured on various scales has led to considerable confusion (Kochanek 1996; Zaritsky 1999). More important, the modeling which is required to make dynamical measurements of mass becomes increasingly uncertain on large scales, where dynamical time scales can exceed the Hubble time. For these

reasons, it is essential to pursue alternative approaches.

Einstein's theory of general relativity predicts that the path of a light ray will be deflected as it passes through an inhomogeneous mass distribution. The effects created by these deflections, referred to as gravitational lensing, provide an alternate approach to determining the distribution of mass in the Universe. The gravitational lensing effect created by an astrophysical object depends on both the density contrast within it and the geometry of the lensing system. It is completely independent of the dynamical state or nature of the matter in the lens.

Gravitational lensing is detected by measuring the effect of nearby 'lens' objects on the observed shapes of more distant 'source' galaxies. The effects caused by high density lenses can be spectacular, including both multiply imaged sources (Walsh, Carswell, & Weymann 1979) and highly distorted giant arcs (Lynds, & Petrosian 1986). In these cases of dramatic distortion, the lensing masses of individual objects can be traced in detail. Unfortunately such strong lensing occurs only in very rare, high density contrast regions.

The density contrast in the outer regions of galaxies and clusters is very small. As a result, the lensing distortions they introduce can be tiny, often smaller than 1%. The source galaxies we observe have unknown intrinsic shapes and these weak lensing effects can only be observed statistically (Tyson, Valdes, Jarvis and Mills 1984; Webster 1985; Tyson, Wenk, & Valdes 1990). By measuring the average distortion in the shapes of a large number of background galaxies, we can determine the effect of a lens. This weak lensing technique depends on the assumption that alignments of source galaxies are produced only by intervening lenses (Tyson 1985). Source galaxies seen as close to a lens in angle are usually separated from the lens by large distances along the line of sight, so this assumption is not unreasonable.

In the case of galaxies, the effect of a single lens is too small to be measured accurately using the limited number of source objects available behind it. In this case we can still measure the *average* lensing effect of a set of lenses by 'stacking' the lens objects. This is fundamentally the same as measuring the objects individually (at very low signal-to-noise) and combining the measurements. This technique of stacking lens objects was first performed for galaxy-galaxy lensing studies (Tyson, Valdes, Jarvis and Mills 1984; Brainerd, Blandford and Smail 1996; Fischer, et al. 2000; Smith, et al. 2000; Wilson, Kaiser, & Luppino 2000). Its use has now been extended to the statistical study of galaxy groups (Hoekstra, et al. 2001) and clusters (Sheldon, et al. 2001).

These statistical measures have often been considered as measurements of the average lensing mass of a class of galaxies. This interpretation is complicated by the intrinsic clustering of galaxies (Fischer, et al. 2000; Seljak 2000) and by the fact that galaxies can be found in a range of halo masses. On larger scales groups and clusters can dominate the signal and since there are typically many galaxies inside such halos, only one of which can be at its center, one has to be careful with this interpretation. Another way to say this is that lensing masses measured on ≥ 100 kpc scales include contributions from both the central galaxy being studied and its neighbors, all of which could be embedded in a larger mass concentration or could be clustered in the field.

Interpretation of lensing measurements is simplified by recognizing that traditional galaxy-galaxy lensing studies really measure the correlation between a set of points (galaxy locations) and the mass which surrounds them. This galaxy-mass correlation function (GMCF) is very well defined, and it can be directly compared to the results of N-body simulations or to other theoretical models just like the galaxy correlation function. In this view the correlation of mass with a galaxy and the correlation of galaxies with one another can be viewed as related, but not identical, clustering statistics, both of which in turn are related, but not identical, to dark matter clustering. This view is most useful on large scales, where the constant bias assumption is most reasonable. Here we will for the most part stick to the classical interpretation of galaxy-galaxy lensing as measuring dark matter halos around galaxies, but we will also comment on what this really means in light of more realistic models.

In this work we use gravitational lensing techniques to measure the galaxy-mass correlation function for a large magnitude limited sample of lens galaxies. We combine the derived GMCF with measurements of the optical luminosity associated with these objects in five optical passbands. These measurements allow us to study the relation between mass and light for galaxies covering a wide range in luminosity, galaxy type, and local environment.

This work expands on our initial measurements of the GMCF (Fischer, et al. 2000) in two crucial ways. First, all lens objects used here have spectroscopic redshifts. This allows us to properly combine all lenses, and to place our measurements on a solid physical scale. Second, since the distances to all lenses are known, it is possible to confidently relate the physical properties of the lenses to the lensing signals which they induce.

In §2 we describe the data on which this study is built and in §3 we describe our gravitational lensing mass reconstructions. We present measurements of the GMCF in §4, and probe its dependence on luminosity, galaxy type, and environment. In §5 we compare aperture mass and luminosity measurements to study the relationship between M/L and various galaxy properties. We discuss the results in §6. We conclude in §7 with a description of future extensions of these measurements, both to higher accuracy, and to new approaches. Throughout this work we use $H_0 = 100$ h km s^{-1} Mpc^{-1}, $\Omega_m = 0.3$, and $\Omega_\Lambda = 0.7$.

2. OBSERVATIONS

The analyses reported in this work are based on observations obtained by the Sloan Digital Sky Survey[16]. The SDSS includes both imaging and spectroscopic surveys (York et al. 2000) of approximately 10^4 square degrees in the North Galactic Cap. The SDSS telescope (Siegmund, et al. 2001) is a dedicated 2.5 m f\5 survey telescope with a flat, essentially undistorted 3° field of view. Two instruments, a large imaging camera (Gunn, et al. 1998) and a 640 fiber plugger plate multifiber spectrograph (Uomoto, et al. 2001) alternate in the focal plane of the telescope. Imaging data is taken only when conditions are optimal

---

[16] www.sdss.org

(photometric skies, no moon, and seeing $<1.5''$). Spectroscopic data are obtained during the remaining time. Imaging data are acquired in drift scan mode, providing near-simulataneous observations in five bandpasses (u', g', r', i', and z' (Fukugita, et al. 1996)) to a limiting magnitude of about $r^* = 23.0$. The pixel scale for imaging observations is $0.396''$ per pixel, allowing Nyquist sampling for $1.0''$seeing. Spectroscopic targets selected from these images are observed with the multifiber spectrograph beginning in the month following imaging observations. The spectra obtained cover a wavelength range from 390 to 910 nm with a resolving power of $\sim$2000. Typical S/N for SDSS spectra is $>$100 per pixel. The SDSS will ultimately image more than 10^8 galaxies, and obtain spectra for more than 10^6 galaxies and 10^5 quasars. To date the SDSS has obtained imaging data for more than 3000 square degrees, and spectra for more than 150,000 independent objects.

The data used in this analysis are drawn from SDSS commissioning runs. Imaging data were obtained between Fall 1997 and Spring 2000. Seeing in these early runs varied from $1.0''$ to $2.0''$. Spectroscopic targets selected from this imaging data were observed with the SDSS spectrographs over a series of nights during 2000. The SDSS photometric system is not yet finally defined. To remind the reader of this, we refer to all measured magnitudes using the symbols u^*, g^* etc., and to the passbands themselves as u', g' etc.

SDSS imaging data are reduced and calibrated by the SDSS photometric (PHOTO: Lupton, et al. (2001)), astrometric (ASTROM: Pier, et al. (2001)) and calibration (MT: Tucker, et al. (2001)) pipelines. These pipelines begin by cleaning the raw images and obtaining astrometric solutions. They extract objects from the images, deblending them where necessary, measure a wide range of possible properties, and combine the five color data into an extensive photometric catalog of measured object properties. In addition to the parameter catalog these pipelines provide small 'atlas images' extracted from the full images around each objects. They also provide continuous, detailed information about the shape and size of the PSF across the focal plane. We make use of the SDSS measured parameters, the atlas images of objects, and the PSF information to perform the analyses presented below.

Spectroscopic targets are selected from the imaging data in three primary classes; the 'main' galaxy sample, designed for traditional large scale structure studies out to z=0.2, a 'luminous red galaxy' (LRG) sample, designed to probe peaks of the density field to z=0.5, and a quasar sample. We concentrate in this work on the 'main' galaxy sample, which accounts for about 80% of SDSS spectroscopy. These objects are selected by requiring that they be well resolved and have reddening corrected (Schlegel, Finkbeiner, and Davis 1998) Petrosian magnitudes (see below) brighter than r^*=17.6. Details of the spectroscopic target selection for the SDSS main galaxy sample will be discussed in Strauss, et al. (2001).

The spectra for these objects were reduced by the SDSS spectroscopic pipeline (SPECTRO: Frieman, et al. (2001)). This pipeline extracts 1D spectra from the 2D spectrograph images, calibrates them, and measures redshifts by cross-correlation with stellar templates. Redshifts are determined for about 98% of all galaxy targets, with a typical velocity accuracy of $<$30 km/s.

2.1. *Lens and source galaxy selection*

To conduct our lensing mass measurements we divide the observed sample of galaxies into a foreground lens sample and a background source sample. For lens galaxies we select only SDSS main galaxy targets for which spectroscopy is complete. As a result, every lens object has a measured spectroscopic redshift. This is essential for the accuracy of our lensing analysis. It allows us to tightly constrain the geometry of each lens and to appropriately rescale all of our lensing measurements before we combine them.

The selection of galaxies used here is very similar to that used in the first determination of the SDSS luminosity function described in Blanton et al. (2001). The magnitude and redshift distributions for this lens sample are shown in Figure 1. The photometric accuracy of this bright sample is limited solely by systematic calibration uncertainty of $\sim$3%. The total number of lens galaxies available for these studies is 34693.

Because of the physical size of the fiber holes in the spectrograph, it is impossible to obtain spectra for two galaxies closer than $55''$ within one spectroscopic plate. Spectra are obtained for some of these galaxies by overlapping spectroscopic plates, but a small fraction ($< 5\%$) remain unobserved. While these galaxies are not analyzed as lenses, we do keep track of them in the studies of lens angular clustering described below.

The source galaxy sample is assembled with two requirements in mind. First, source objects should be behind the lens galaxies. Since we lack spectroscopic redshifts for these fainter objects, we begin by selecting all galaxies fainter than r^*=18. To be useful for lensing, we must be able to accurately measure the shapes of source galaxies. It is impossible to accurately measure the shape of any object which is not well resolved. The shape measured for objects which are smaller than the PSF is merely the shape of the PSF. Accurate shape measurement also requires relatively high signal-to-noise (a $>$10σ detection). As a result we select as source galaxies well resolved objects with r^* from 18.0 to 22.0. More details of the selection are given below.

A total of 3,615,718 source galaxies are available for these studies. Figure 1 illustrates the source magnitude and estimated redshift distribution. Estimation of the source redshift distribution is described in §3.3. Since the g', r', and i' passbands are substantially more sensitive than u' and z', we will conduct all our shape measurements of source galaxies in these three central bands. The u' and z' data for the relatively bright lens galaxies are, however, excellent. So we will use u' and z' data in understanding lens properties.

2.2. *Lens luminosity measurements*

Luminosities for the lens galaxies are derived by combining the PHOTO measurements of light profiles in five colors with the redshifts determined by SPECTRO. Since galaxies have a variety of luminosity profiles and lack well-defined boundaries, determining their total flux is complex and model dependent. Traditional aperture and isophotal flux measurements are plagued by well known biases

with redshift and galaxy type. As a result the SDSS has adopted a circular aperture flux measurement in which the radius of the aperture selected is adapted to the shape of each galaxy's light profile.

The basic measurement of galaxy luminosity for the SDSS is a Petrosian (1976) magnitude. For the SDSS, the Petrosian radius is defined as the largest radius at which the local surface brightness is one eighth of the mean surface brightness interior to that radius. The Petrosian flux is then the total flux within a circular aperture with radius two times the Petrosian radius. Technical details of this Petrosian flux measurement are presented in Lupton, et al. (2001). An extensive discussion of the fraction of total light measured for various model galaxy profiles is given in Blanton et al. (2001). The SDSS Petrosian magnitude detects essentially all the light (>97%) from galaxies with exponential profiles, and more than 80% of the light from galaxies with de Vaucouleurs profiles.

Conversions from apparent magnitude m to absolute magnitude M depend on cosmology through the distance modulus DM(z) and on galaxy type through the K-correction K(z). Absolute magnitudes are defined by the relation:

$$M = m - DM(z) - K(z) \qquad (1)$$

In this work we consider only a FRW cosmology in which Ω_m=0.3 and Ω_Λ=0.7 with a Hubble constant $H_0 = 100h$ km s^{-1} Mpc^{-1}. The distance modulus is then determined from formulae summarized in, for example, Hogg (1999). K-corrections are applied to correct for the difference between observed passbands and rest-frame passbands. Given the redshift and observed g^*-r^* color of each galaxy, we determine a best fit K-correction by interpolation from the tables supplied by Fukugita, Shimasaku, and Ichikawa (1995).

Luminosity distributions for all the lens galaxies in the sample are shown in Figure 2, along with the values of M* derived from SDSS measurements of the luminosity function (Blanton et al. 2001).

2.3. Lens galaxy classification

As a part of this study, we will examine correlations between mass, luminosity, and lens galaxy type. To enable this we have conducted a simple automatic classification of all the lens galaxies in our sample. This classification is based on a combination of SDSS PHOTO parameters and reanalysis of lens atlas images. The goal of this classification is to place galaxies along a continuous sequence from early type 'ellipticals' to late type 'spirals'.

Previous studies of automatic galaxy classification (Abraham et al. 1994; Bershady, Jangren, & Conselice 2000) have shown that parameters such as concentration, color, and rotational asymmetry correlate well with morphology or Hubble type. Concentration and color computed by PHOTO have been shown to correlate well with morphological type by Shimasaku et al. (2001) and Strateva et al. (2001). For this study we combine three parameters for galaxy classification: the g^*-r^* color, a measure of concentration, and a measure of asymmetry.

The g^*-r^* color has been shown by Strateva et al. (2001) to correlate well with morphology for all galaxies within the redshift range of our lens sample. For galaxies at higher redshift (beyond z∼0.38), the 4000 Å break passes

from the g' to the r' band, and classification must consider the r^*-i^* color. We define a concentration parameter from PHOTO outputs by comparing $r^p_{50}(r')$, the Petrosian half-light radius, and $r^p_{90}(r')$, the radius at which 90% of the r' Petrosian flux is contained. Our concentration is the ratio of these two.

Unlike the rotational symmetry measurements used by Abraham et al. (1994), we employ a bilateral asymmetry measurement. It is more sensitive than rotational symmetry to localized features because it does not dilute them as strongly. This asymmetry measure is also model independent. Our asymmetry parameter is not measured in the standard PHOTO processing of SDSS data. To make the measurement we refer to the 'atlas images' of each object. After finding the major axis of the light distribution of a galaxy, we subtract the galaxy light on one side of the image from the light on the other. The asymmetry is then defined as:

$$Asymmetry = \frac{\Sigma Residuals\ from\ Subtraction}{\Sigma Flux\ before\ Subtraction} \qquad (2)$$

This parameter is small for galaxies with smooth, symmetric light profiles and large for galaxies which are lumpy or otherwise asymmetric. Because of the abundance of blue light emitted in star forming regions, we measure this asymmetry in the g' band.

Correlations among these three classification parameters are shown in Figure 3. Concentration and color contain most of the classification information, though the asymmetry parameter adds some discrimination among types. These three classification parameters are scaled to their approximate range and combined in quadrature to produce a single classification parameter which varies from zero to one. This classification is not intended to place galaxies along a Hubble sequence, but merely to separate late types from early types in a statistical way. Nevertheless, we find that our classification correlates well with the visual classification of 456 bright SDSS galaxies reported by Shimasaku et al. (2001). We will later divide the lens catalog into subsets using this classification parameter.

3. LENSING MASS MEASUREMENTS

When light from a source galaxy passes near a lens, its path is deflected. If the surface density of the lens is decreasing with projected radius, the effect of lensing in the weak regime is to stretch the images of background galaxies in the tangential direction. There is a simple relation between the tangential shear and the mass density contrast:

$$\gamma_+(R) = \overline{\kappa}(\leq R) - \overline{\kappa}(R) \qquad (3)$$

where γ_+ is the shear in the tangential direction, and $\kappa = \Sigma/\Sigma_{crit}$ is the surface density of the lens measured in units of the critical density. The critical density is dependent in an important way on the geometry of the lens-source system:

$$\Sigma_{crit} = \frac{c^2}{4\pi G}\frac{D_S}{D_L D_{LS}} \qquad (4)$$

where D_S and D_L are the angular diameter distances to source and lens, respectively, and D_{LS} is the distance from source to the lens.

If the lens geometry is known, measurements of the tangential shear can be converted directly to measurements of surface mass density contrast in the lens:

$$\gamma_+(R)\Sigma_{crit} = \overline{\Sigma}(\leq R) - \overline{\Sigma}(R) \equiv \Delta\Sigma_+ \qquad (5)$$

This measured mass density contrast can then be either integrated or, more often, fit to a model profile, to constrain the mass of a lens object. For the case of an isothermal mass profile ($\Sigma(R) \propto R^{-1}$), the density contrast $\Delta\Sigma_+$ is equal to the density itself. This surface mass density contrast is what we refer to in this work as the galaxy-mass correlation function.

Two measurements are essential to lens reconstruction; the tangential shear $\gamma_+(R)$ produced by the lens as a function of radius, and the geometry of the lens system as encoded in Σ_{crit}. Both are described in detail in what follows.

3.1. Measurement of galaxy shapes

The first step in measuring tangential shear is measurement of the source galaxy shapes. To improve the S/N of these shape measurements beyond those provided by the SDSS pipelines, we re-measure all object shapes from the atlas images using an adaptively weighted moment scheme (Bernstein, et al. 2001). We measure quadratic moments ($Q_{i,j}$) of the galaxies weighted by an elliptical Gaussian matched in location, size, and orientation (by an iterative procedure) to that of the object being measured:

$$Q_{i,j} = \frac{\sum_{k,l} I_{k,l} G_{k,l} x_i x_j}{\sum_{k,l} I_{k,l} G_{k,l}} \qquad (6)$$

where $I_{k,l}$ is the sky subtracted surface brightness of pixel (k,l), $G_{k,l}$ is the Gaussian weight evaluated at pixel (k,l), and x_i is the pixel offset from the image centroid. From these moments we define the ellipticity components, or polarization, (Blandford, et al. 1991):

$$e_1 = \frac{Q_{1,1} - Q_{2,2}}{Q_{1,1} + Q_{2,2}}$$
$$e_2 = \frac{2Q_{1,2}}{Q_{1,1} + Q_{2,2}} \qquad (7)$$

These ellipticity components are related to the more familiar major axis (a), minor axis (b), and position angle (β) as:

$$(e_1, e_2) = \frac{a^2 - b^2}{a^2 + b^2}(\cos 2\beta, \sin 2\beta) \qquad (8)$$

The measured shapes of these objects are then corrected to remove the effects of seeing and an anisotropic PSF as described in Fischer, et al. (2000). There are two important effects in SDSS data. The isotropic part of the PSF (mostly seeing) tends to circularize or dilute the observed shapes of galaxy images. The sensitivity of a galaxy to this circularization is called its "smear polarizability" S_m, which depends primarily on the ratio of PSF size to galaxy size. An object which is smaller in size than the PSF width has S_m approaching one. It is impossible to measure ellipticity of such objects, as they are unresolved. An object which is large compared to the PSF has S_m approaching zero. We can measure the shapes of such large objects very accurately, independent of the size of the PSF. Though the smear polarizability is mostly due to object size, it is also

somewhat dependent on profile shape (Bernstein, et al. 2001).

The real shape of a galaxy is related to its measured shape by dividing its ellipticity components e_i by a dilution correction ($1 - S_m$). When S_m is large, this correction becomes large and ill determined. As a result, we limit our selection of source galaxies to those objects for which S_m is less than 0.8. This is also an effective star-galaxy separation technique.

In addition to the isotropic part of the PSF, which dilutes the observed shape of an object, anisotropic components of the PSF induce ellipticity in an object's shape. The induced ellipticity is directly proportional to the ellipticity of the PSF. Because this effect is a convolution of the true image with the PSF, it will be strong for objects comparable in size to the PSF and weaker for larger objects. Again, it is approximately the ratio of PSF size to object size that is the important factor. We correct for PSF anisotropy by subtracting off the PSF shape weighted by the smear polarizability. The corrected shape of each galaxy is then given by:

$$e_i(corrected) = \frac{e_i(observed) - S_m * e_i(PSF)}{1 - S_m} \qquad (9)$$

SDSS observations are obtained continuously, in drift scan mode. During the night the PSF varies for many reasons, including changes in atmospheric seeing, focus, and anomalous refraction. As a result, the PSF must be carefully tracked throughout the data so that the appropriate form can be used to correct each galaxy. This is a problem which is aided by the relatively shallow nature of the SDSS. The numbers of observed stars and galaxies here are similar. In very deep lensing studies galaxies greatly outnumber PSF stars. PHOTO tracks the PSF as a function of position and time using the large number of stars in each image, allowing accurate PSF reconstruction at the position of each galaxy (Lupton, et al. 2001).

3.2. Shear Measurements

Lensing induces tangential shear in the images of background source galaxies. As long as the orientation of the distant source galaxies is otherwise independent of the foreground lens, one can measure the induced shear directly from the shapes of source galaxies. For the special case of weak lensing ($\kappa \ll 1$), this induced shear is just half the induced tangential ellipticity (Miralda-Escudé 1991). We denote this tangential component of the ellipticity as e_+ and the orthogonal, 45 degree component of the polarization as $e_\times$.

Because galaxies have intrinsic shapes, and the lensing effect we are measuring is weak, the shape of a single galaxy gives a very noisy estimate of the shear. In order to increase the signal to noise, we average the tangential shapes of source galaxies in bins of radial separation from the foreground lens:

$$\hat{\gamma}_+ = \frac{1}{2S_{Sh}} \frac{\sum w_i e_+^i}{\sum w_i}, \qquad (10)$$

where the w_i are the weights for each measurement. S_{sh} is the average responsivity of the source galaxies to induced shear (see below).

There are two dominant sources of random noise in shear measurements: the intrinsic variance in galaxy shapes, or

"shape noise", and the uncertainty in the shape measurement of each galaxy. The mean variance in galaxy ellipticity, determined from well measured SDSS galaxies is $\sigma_{SN} = \langle e_i^2 \rangle \sim 0.32$, and the typical shape measurement uncertainty is $\sigma_i \sim 0.25$. For optimal S/N we weight the contribution of each source galaxy by $w_i = 1/(\sigma_i^2 + \sigma_{SN}^2)$.

The shear responsivity measures the efficacy with which an applied lens shear can alter the observed shape of a galaxy, and is simular to the shear polarizability defined in Kaiser, Squires, & Broadhurst (1995). If a galaxy is perfectly tangentially aligned, and has an ellipticity of 1, it cannot be made to appear more tangentially aligned by the lens. We measure the responsivity for the ensemble of sources using the method of Bernstein, et al. (2001):

$$ S_{sh} = \frac{\sum_i [w_i(1 - \sigma_{SN}^2 w_i e_+^2)]}{\sum_i w_i} \qquad (11) $$

Combining this measure of shear responsivity with the weights described above yields a measurement of mean shear as a function of angle from the lens center.

3.3. Accounting for lens geometry

To convert this measurement of shear as a function of angle to a measurement of mass contrast as a function of physical radius we have to account for the lens geometries. The conversion from angular separation to projected physical separation requires only application of the angular diameter redshift relation.

To place our measurements on an accurate mass scale we must determine a mean Σ_{crit} for each lens. We do this by combining the measured lens redshifts with the overall redshift distribution of the background galaxies.

$$ \Sigma_{crit}^{-1}(z_L) = \int_{z_L}^{\infty} \Sigma_{crit}^{-1}(z_L, z_s) P(z_s) dz_s \qquad (12) $$

Where $P(z_s)$ is the normalized source redshift distribution.

To estimate the source redshift distribution we gather a sample of galaxies with spectroscopic redshifts and accurate photometry. Two samples are combined. For galaxies brighter than $r^* = 17.6$, we use our own SDSS lens galaxy sample. For galaxies fainter than $r^* = 17.6$, we use galaxies drawn from the Canada-France Redshift Survey (CFRS: Lilly et al. (1995)). CFRS galaxies have magnitudes measured in V and I. We convert these to r^* using the relation

$$ r^* = I_{CFRS} + 0.5(V_{CFRS} - I_{CFRS}) \qquad (13) $$

This relation is empirically determined from 61 galaxies observed by both SDSS and CFRS. This direct comparison automatically accounts for average differences between the isophotal photometry of CFRS and the Petrosian photometry of the SDSS. The combined sample gives us a list of calibration galaxies with spectroscopic redshifts spanning a range from $r^* = 14$ to $r^* = 23$.

To estimate the source redshift distribution as a function of magnitude we fit the redshift distributions of the calibration galaxies, in bins of r^*, to the function (Baugh & Efstathiou (1993))

$$ n(z) = \frac{3z^2}{2z_c^3} \exp\left(-\left(\frac{z}{zc}\right)^{3/2}\right) \qquad (14) $$

The fit values of z_c in each r^* bin are then used to derive a relationship between r^* and z_c. We combine this relation with the observed r^* magnitude distribution of the

source galaxies to obtain a source galaxy redshift distribution. The relation between r^* and z_c is shown in Figure 4. As an illustration of the effectiveness of this method we compare real and estimated redshift distributions for CFRS galaxies in Figure 5.

It is worth noting that, since the CFRS is complete to m_I of 22.5, no extrapolation of the $r^* z_c$ relation to magnitudes fainter than the calibration are required. Lens geometries are, on average, understood very well for this analysis. In addition, since the mean number of source galaxies per lens is $\gtrsim 100$, each lens samples this distribution relatively well.

The inferred source redshift distribution is shown in figure 6(a). The effect of geometry on a lens can be expressed as a "lensing strength" characterized by Σ_{crit}^{-1}. Where Σ_{crit} is small, so that Σ_{crit}^{-1} is large, lensing effects will be large. The mean lensing strength as a function of lens redshift, shown in figure 6(b), is calculated from the source redshift distribution using equation 12. Distributions of both are shown for g', r', and i' because the source samples in each band are slightly different.

3.4. Combining lenses

The sensitivity of shear measurements goes as $\sigma/\sqrt{N_{source}}$ where $\sigma = \sqrt{\sigma_{sh}^2 + \sigma_{meas}^2} \sim 0.4$. The maximum ellipticity induced by a SDSS foreground galaxy on background sources is very small, $\lesssim .005$ (Fischer, et al. 2000). At least 10 thousand source galaxies are required to measure such a small signal. SDSS images, however, typically have ~ 2 sources per square arcminute, or about 650 within a $600''$ aperture. This is too few sources to measure the shear from a single galaxy with precision. In order to obtain the required number of sources, we combine the signal from many lenses.

Care must be taken when combining the shear measurement from lenses at different redshifts. As equation 3 suggests, the shear depends upon the redshift of the lens and source. If we wish to combine lenses, we must combine measurements of density contrast (Equation 5) rather than measurements of shear (Equation 3). Note that the weights used in equation 11 must also be rescaled to $W_i = w_i \Sigma_{crit}^{-2}$.

On average, equation 12 accounts for the geometry of the lens-source system, including the fact that some sources are actually in front of the lens and are not lensed. This average relation does not, however, account for the intrinsic clustering of galaxies. Some of the sources are faint neighbors physically associated with the lens galaxies. These faint neighbors are not lensed. Because their number density is a decreasing function of distance from the lens center, this will produce a radial bias in the shear estimate. A comparison of the number density of sources around lenses to the number density around random points gives an estimate of the mean number of faint galaxies associated with the lenses.

This dilution effect can be corrected for by multiplying the mean density contrast by a radial correction factor $F(r) = \langle N_{lens} \rangle / \langle N_{rand} \rangle$, the ratio of source galaxies around lenses to that around random points. We chose 155,000 random points (5 random points for each lens), spread uniformly through out the same areas sampled by the lenses and drawn from the same redshift distribution

as the lenses, in order to measure the mean background density correctly. The correction F(r) varies from 6% at 70 h^{-1} kpc to 0.04% at 940 h^{-1} kpc.

4. THE GALAXY-MASS CORRELATION FUNCTION

The ensemble density contrast measured around the lens galaxies is shown in Figure 7. Measurements based on source galaxy shapes in each of the three most sensitive bandpasses are shown. These profiles include corrections for the shear responsivity as well as the correction for the inclusion of faint neighbors in the source galaxy sample discussed above. Only lenses which were surrounded by a reasonably symmetric distribution of source galaxies were used. This check is done to allow residual correlations in source galaxy shapes to cancel as they are projected tangentially around the lens centers. The final sample includes 31,039, 31,174, and 31,203 lens galaxies for the g', r', and i' measurements, respectively.

Figure 7 also shows a the measurement of the GMCF obtained by combining the measurements made in g', r', and i'. Lensing measurements made in these three bands are not entirely independent. First, they measure shapes of the same source galaxies. While the intrinsic shapes of these galaxies are not exactly the same in these different bands, they are strongly correlated. So the shape noise in these three measurements is related. While each color has a PSF shape independent of the others, the time variation of the PSF (which is largely a global, seeing effect) is correlated among the bands. As a result, the combination of the three bands requires consideration of the correlation matrix among the colors, and yields gains in S/N which are less than the optimal $\sqrt{3}$.

The density contrast measurements displayed in Figure 7 are fit to a power law model of the form:

$$\Delta\Sigma_+ = A \left(\frac{R}{1 \text{ Mpc}} \right)^{-\alpha} \qquad (15)$$

Best fit values for the normalization A and the power law index α are given for each color, and the combined measurement, in Table 1. The χ^2 statistic for the combined data was estimated using the full covariance matrix; χ^2 contours for these best fits are shown in Figure 8. The best fit to the combined GMCF is

$$\Delta\Sigma_+ = (2.5^{+0.7}_{-0.6}) \left(\frac{R}{1 \text{ Mpc}} \right)^{-0.8\pm0.2} h\text{M}_\odot\,\text{pc}^{-2} \qquad (16)$$

When we study the variation of the GMCF with luminosity in §4.2 we will fix the power law index α to this best fit value of 0.8 and allow the normalization A to vary. All subsequent measurements of the GMCF discussed in this work are made from the combined g', r', and i' data for maximum S/N.

This measurement of the mean density contrast averages over galaxies of many different types, drawn from many different environments. In this sense, the mean density contrast is really a measurement of the projected galaxy-mass correlation function (GMCF). Included in this profile is not only the lensing induced by the central galaxy, but also the effect of all the neighboring lenses either in projection or physically associated with the central galaxy.

4.1. Checks of the GMCF

As a simple test to see if our signal is due to gravitational lensing we rotate the orientation of all source galaxies by 45 degrees and measure the orthogonal of the density contrast, which we will denote as $\Delta\Sigma_\times$. This is equivalent to measuring the curl of a gradient and should be zero (Kaiser 1995) for any real shear signal. This measurement is shown in Figure 9 in the same radial bins as the measurement of $\Delta\Sigma_+$.

A very powerful check of the level of our systematics can be done by measuring the shear around random points. This test is possible because the SDSS observes large contiguous regions of sky. There should be no correlation between source galaxy shapes and these random points, and the resulting tangential shear should be consistent with zero. We use the 155,000 random points discussed in §3.4 to make this measurement. The result, shown in Figure 10, is consistent with zero, and far below the measured signal.

These results demonstrate that the shape correlation which appears in our measurement of the galaxy-mass correlation function (Figure 7) is consistent with lensing. There is no net tangential alignment of background galaxies detected unless you measure its correlation with the location of foreground lenses.

If the formation of luminous galaxies is at all affected by the dark matter environment in which they form, there should be relationships between the luminous properties of galaxies and their GMCF. The following sections present measurements of the dependence of the GMCF on galaxy luminosity, morphology, and local density. They show strong changes in the amplitude and in some cases the shape of the GMCF as the luminous properties of the lens sample are varied.

4.2. Dependence of the GMCF on lens galaxy luminosity

We begin by probing the scaling between galaxy luminosity and the GMCF. Since the SDSS provides five color photometry, and because we have spectroscopic redshifts for every lens galaxy, we can divide the lens sample by luminosity in each of the five SDSS bands. For each band, we split the lens sample into four luminosity bins.

Because of the shape of the galaxy luminosity function (Blanton et al. 2001), we expect a large number of low luminosity galaxies, and relatively small numbers of high luminosity galaxies. This provides greater lensing sensitivity for low luminosity galaxies. Since we expect these to have smaller masses, we will need this higher sensitivity. We choose a division of the lens galaxies which is uneven in number. This is appropriate for obtaining comparable signal to noise in each bin. Luminosity bins are chosen to give a similar division of the total number of galaxies in each of the five colors; e.g. the third luminosity bin has approximately the same number of galaxies in the u^* binning as the r^* binning. Mean luminosities in each bin are calculated using the same relative weighting used in the lensing measurements $(N_{sources} * \Sigma_{crit}^{-2})$.

Figures 11 through 15 show the GMCF split into these four luminosity bins, using u^*, g^*, r^*, i^*, and z^* luminosities respectively. The vertical scale of these plots varies to accomodate the large change in the amplitude of the GMCF between bins, especially in the redder bands. In each case, we present the GMCF measured from a combi-

nation of all three source passbands. The GMCF in each luminosity bin is fit to the model GMCF obtained for the total data set:

The plots are labelled with their mean luminosity in that band, as well as a normalization of the GMCF from fits to a power law with index -0.8, the best-fitting power law index for the entire sample.

There is a strong increase in the amplitude of the GMCF with g^*, r^*, i^*, and z^* luminosity, but there is little correlation between the GMCF and the u^* luminosity. Put another way, the luminosity of galaxies measured in redder bands is strongly related to the dark matter environment in which they form, while the u^* luminosity is not. This is probably not surprising. The u^* luminosity is primarily due to small scale, relatively brief episodes of recent star formation, while the r^*, i^*, and z^* luminosity arises from the integrated star formation history of the galaxy. It appears that this integrated star formation history is much more closely related to a galaxy's dark matter environment than its recent star formation history.

Table 2 presents the essential data. For each luminosity bin, in each color, we supply the number of galaxies used, the mean luminosity of the galaxies, and the measured density contrast in the annulus $20 \leq R \leq 260\ h^{-1}$ kpc. While the amplitude of the GMCF is increasing strongly with luminosity, the number of available lenses is decreasing, so that the S/N of our GMCF measurement is very similar in each of our four luminosity bins (with the exception of u^*). Note that we observe no significant change in the *shape* of the GMCF with luminosity, only the amplitude is seen to change.

4.3. *Dependence of the GMCF on lens galaxy type*

We have also examined the dependence of the GMCF on galaxy type. Galaxies are divided into an early type 'elliptical' sample and a late type 'spiral' sample as described above in §2.3. The sample used includes 13,882 objects classified as spirals and 14,156 classified as ellipticals. The relatively large fraction of elliptical galaxies is due to the magnitude limited SDSS spectroscopic target selection.

The GMCF measured for each of the two samples is shown in Figure 16. Power law fits to these measured GMCFs are given in Table 1. The amplitude of the GMCF for elliptical galaxies is substantially larger than that for the spirals. The shapes of these two GMCFs are consistent, although there is some evidence for environmental effects at large radii (see §4.4). It is important to stress that the GMCF is a redshift independent quantity, unlike the induced shear. Thus the observed discrepancy in central values of the GMCF between spirals and ellipticals reflects a real difference in mass.

This measurement indicates that low redshift elliptical galaxies reside in halos which are substantially more massive than those of spirals. This is perhaps consistent with a picture in which elliptical galaxies form in the merger of two or more *comparably massive* objects (Barnes 1999; Burkert & Naab 2000) and so tend to be found in more massive halos. Thus elliptical lenses will reside in locations with particularly strong GMCFs. While these ellipticals are on average more massive than the spirals, they are also more luminous. Details will be given in §5.

4.4. *Dependence of the GMCF on lens galaxy environment*

In an effort to understand the relationship between GMCF and the environment of the lens galaxy, we have measured the GMCF as a function of local lens density. To do this, we generate a Voronoi tesselation (Icke & van de Weygaert 1987; Ling 1987) around the locations of the lens galaxies. The Voronoi tesselation divides the plane of galaxy locations into polygons. Each point in the polygon which contains a lens is closer to *this* lens than to any other. Hence each Voronoi polygon reflects the area 'owned' by this lens. The inverse of the area of each Voronoi polygon is a reflection of its local density. Small Voronoi polygons occur in the regions of largest local galaxy density.

We divide the lenses into equal samples drawn from overdense and underdense regions and measure the GMCF for each. The resulting GMCFs are shown in Figure 17. While the comparison of spirals and ellipticals showed us a variation in the GMCF amplitude with no change in shape, the comparison of samples drawn from dense and underdense regions shows a variation in GMCF *shape*, with no significant change in the central amplitude. Parameters for best fit power laws to these GMCF measurements are given in Table 1. The inner parts of the GMCF for these two samples are statistically equivilant. They differ only in their outer regions, where the GMCF measured in dense regions is substantially larger.

The dense and underdense samples include lens galaxies whose intrinsic properties (luminosity and morphological type) are very similar. The mean i^* luminosity of the two samples is 2.0 and $2.1 \times 10^{10} L_\odot$ respectively. These lenses differ significantly only in their surroundings. The similarity of their observed GMCFs at small radii suggests that this inner part of the GMCF is primarily associated with the central galaxy. The differences observed at large radii are due to the presence of many more neighbors around the galaxies drawn from the dense sample.

These comparisons provide important clues to interpretation of the GMCF. The central parts of the GMCF are dominated by mass associated with the central galaxy. The outer regions (beyond $\sim 300\ h^{-1}$ kpc) are increasingly affected by the presence of neighboring objects, and hence depend on the properties of the central galaxy in at most a second order way.

5. APERTURE MASS MEASUREMENTS AND MASS-TO-LIGHT SCALINGS

We have seen in the previous sections that the amplitude of the GMCF is strongly dependent on lens luminosity and type, and that the shape of the of the GMCF, especially beyond $\sim 300\ h^{-1}$ kpc is affected by the local environment of the lens. The arguments presented in §1.1 suggest that it is inappropriate to attempt to extract the total mass of each lens galaxy. Keeping all this in mind, we will quantify the scaling between GMCF and lens luminosity in the following simple way.

We define an aperture mass (M_{260}) for each class of lens objects by fitting its GMCF to a projected singular isothermal sphere (SIS) model. We simply fit a one parameter

model to the density contrast in the aperture:

$$\Delta\Sigma(R)_{SIS} = \Sigma(R)_{SIS} = \frac{\sigma_v^2}{2G}\frac{1}{R} \qquad (17)$$

where σ_v is the central line of sight velocity dispersion. This density is then integrated to find the mass within the aperture. This is not simply the mass associated with the central galaxy, but should instead be thought of as the normalization of the GMCF.

As the outer regions of the GMCF are strongly affected by neighbors of the lens galaxy, we restrict this fit to the central 260 h^{-1} kpc; the inner three bins in our GMCF (the normalization A discussed in §4.2 was derived from fits to the entire profile). We compare this aperture mass (M_{260}) to the lens luminosity to derive a mass-to-light scaling relation in each of the five bands.

At present the data do not allow one to distinguish between SIS and more realistic profiles NFW profiles (Navarro, Frenk, & White 1997), as both provide adequate fits to the observations. NFW profiles decline more rapidly at large radii, because the outer slope of NFW profile approaches R^{-2}, but the error bars are still large there. Moreover, in this region the contribution from individual halos becomes small compared to the contribution from halos with multiple galaxies or from nearby clustered galaxies in separate halos. The main difference between SIS and NFW is that in SIS model the mass of the galaxy increases with radius more rapidly than in NFW. If we fix the amplitude of GMCF for the two models at $100h^{-1}$kpc, then we find that at $260h^{-1}$kpc SIS overestimates the mass by a factor of 2 relative to the virial mass of the NFW halo (defined as the mass within the radius where the mean overdensity is 340 relative to the mean, the value appropriate for the cosmological model with $\Omega_m \sim 0.3$ and $\Omega_\Lambda = 0.7$). One can therefore interpret the masses in table 1 as the virial masses by taking one half of quoted values. For example, the best fitted NFW profile to the overall sample gives a virial mass of $10^{12}h^{-1}M_\odot$, with the corresponding virial radius of $200h^{-1}$kpc.

For each color, we have an aperture mass (or GMCF normalization) and mean lens luminosity for galaxies in each of the four luminosity bins discussed in §4.2. We fit the data in each color to a power law in the form:

$$M_{260} = \Upsilon \times \left(\frac{L_{central}}{10^{10}L_\odot}\right)^{\beta} \qquad (18)$$

Results for each of the five colors are summarized in Figure 18 and Table 2. In this figure, the small inset plots display the aperture mass in units of 10^{12} $M_\odot$ vs. the mean luminosity of the central galaxies in units of 10^{10} $L_\odot$. The strong dependence of M_{260} on luminosity in the g', r', i', and z' bands is apparent. This result was anticipated by predictions based on semianalytic galaxy formation models (Guzik & Seljak 2001). M_{260} shows little dependence on u'. The larger plots show χ^2 contours for the fits to the parameters Υ and β.

A striking result of this analysis is that the relation between M_{260} and luminosity is consistent with linear in all bands but u'. Where this is true, it is sensible to describe the parameter Υ as a mass-to-light ratio $M_{260}/L_{central}$. For u', where mass is clearly not proportional to luminosity, Υ can only be considered as the normalization of this very weak power law fit. This linear scaling (already

hinted at by Smith, et al. (2000)) is in contrast to the naive expectation from the Tully-Fisher or Faber-Jackson relation, which would predict $\beta \approx 0.5$ for SIS.

More realistic models based on NFW profiles can be made consistent with $\beta \sim 1$ (Mo, Mao & White 1998). However, the Tully-Fisher relation does not lead to a unique mass-luminosity relation at the virial radius, because large variations in the deduced virial velocity of the halo at a given observed rotation velocity can conspire to give approximately the same Tully-Fisher relation (Navarro 2001). Galaxy-galaxy lensing provides a much more direct measurement of total galaxy masses at a given luminosity and our results suggest that mass at $260h^{-1}$kpc linearly scales with light at these luminosities (around L_*).

We caution that one must be careful in interpreting $M_{260}/L_{central}$ as the mass to light ratio of the central galaxy. On average, it is contaminated by contributions from neighboring objects at the 10% level (see §5.2 for a description of this estimate). It is also only an aperture measurement, which does not include the total mass of the central galaxy (which may be a poorly defined concept anyways). The value obtained for such an aperture mass-to-light ratio has long been known to be dependent on aperture (Ostriker, Peebles, & Yahil 1974; Zaritsky 1999; Bahcall, et al. 2000). If one is interested in virial mass to light ratios it is best to fit the observations to NFW profiles directly. Since the radii where the data are most sensitive to are close to the virial radius of a $\times 10^{12}h^{-1}M_\odot$ galaxy ($200h^{-1}$kpc) one finds that the virial mass is also approximately linearly proportional to light. $M_{260}/L_{central}$ is also not a mass-to-light ratio which can be simply multiplied by the luminosity density to determine the cosmic mass density by Oort's method. This is because we only determine $M_{260}/L_{central}$ over a narrow range of luminosities and there is no reason why the same value should extend to all the galaxies that contribute to the luminosity function. We plan to investigate mass-to-light ratios by combining measurements of the galaxy-mass correlation function with measurements of the galaxy-luminosity correlation function. This analysis will be presented in a companion paper.

5.1. Aperture mass-to-light scalings and morphology

We showed in §4.3 that the GMCF for ellipticals is significantly stronger than that for spirals. Converting the density contrast to an aperture mass, we find that M_{260} for ellipticals is a factor of 2.7 larger than that for spirals. We compare this mass to the mean luminosity of the lens samples in each of the SDSS bandpasses to obtain a value for $M_{260}/L_{central}$. We lack the signal to noise to confirm that mass is proportional to light in each of these samples.

Results are shown in Figure 19. We find that $M_{260}/L_{central}$ is nearly a factor of four larger for ellipticals than spirals in u', and about a factor of 2.5 larger in g'. In r', i', and z' however, the spiral and elliptical samples show values for $M_{260}/L_{central}$ which are consistent with each other, and with the overall sample. We note that the Petrosian luminosities used by the SDSS systematically underestimate the luminosity of elliptical galaxies relative to spirals by about 20% relative to spirals (see §2.2 and Blanton et al. (2001) for details). Accounting for this makes the $M_{260}/L_{central}$ aggreement in the red bands still

closer.

This reinforces the notion, already suggested in §5, that the relationship between mass and light is particularly simple when observed in red bands.

5.2. *Constraining the mean galaxy halo profile from the galaxy-mass correlation function*

Because the density of lens galaxies on the sky is relatively large, and especially because lens galaxies are themselves clustered, understanding how much of the projected density we measure is primarily associated with each central galaxy is complex (Fischer, et al. 2000; Seljak 2000). The measured density contrast includes contributions from the central galaxy as well as the neighboring galaxies within the aperture. For relatively small radii the projected density is dominated by the central galaxy. As the aperture we study increases, the average contribution of neighbors also increases.

There are three kinds of effects. First, there are neighbor contributions which arise because of the clustering of galaxies in our lens sample. These are galaxies which are comparable in luminosity (and hence probably in mass) to one another. A second kind of neighboring object exists as well; those neighbors which are substantially *less* luminous than our lens sample. Dealing with these galaxies is a definitional problem which lies at the core of this measurement. Finally, the galaxies can also belong to larger structures, such as groups and clusters. There can be mass associated with these structures which is not correlated with individual galaxies.

If we wanted to extract the "total" mass of galaxies from these measurements, we would have to account for all possible lens objects. At some point (at some luminosity) we would have to begin considering faint neighbors as parts of the central lens. As there is no physically motivated scale on which to do this, we must recognize this as a feature of these measurements. Similarly, to include the larger structures we would first need to know their positions and masses, which again is not possible in the absence of additional information such as X-ray emission. As a result most of our analyses treat the GMCF as the fundamental measurement. By explicitly including all the mass correlated with galaxy locations we avoid the conundrum of how to generate a complete sample of lens objects.

We present here a simple analysis designed to assess the importance of the first kind of neighbors; those which are luminous enough to be included in our lens sample. The goal is not to extract isolated "total" masses for lenses, but simply to give the reader an understanding of the effect of lens clustering on the observed GMCF.

We begin by determining the extent of clustering among our lens galaxies. Figure 20 shows the overdensity $\phi(R)$ of neighboring bright galaxies ($r^* \leq 17.8$) around our foreground lens sample (symbols with error bars). The dashed line is the cumulative number of bright neighbors. For this sample, there is on average about 1 neighbor within $275h^{-1}$ kpc. Each of these neighbors contributes to the measured density contrast. The solid line is the best-fitting power law,

$$\phi(R) = \left(\frac{R}{0.94 \mathrm{Mpc}} \right)^{-0.74} \mathrm{Mpc}^{-2} \qquad (19)$$

The data deviate from a power law in the inner bin. We

believe this is due to undeblended neighbors of the central galaxy; see Scranton, et al. (2001) for more details. We note that this is not quite the same as measuring the overdensity of lens galaxies around lens galaxies. For our lens sample we require an SDSS spectroscopic redshift. There are some galaxies which are bright enough to be targeted for SDSS spectroscopy which do not as yet have spectra. While we cannot include these galaxies in our lens sample (it would be impossible to rescale them correctly), we do include them in our measurement of the clustering of lens galaxies.

We follow the method of Fischer, et al. (2000) to account for the presence of the neighboring galaxies. We assume that all the galaxies in the sample have the same halo profile, $\Sigma_g(R)$. We further assume the density of neighbors is given by the overdensity shown in Figure 20. The mean projected mass density of the neighbors can then be written as

$$\Sigma(R)_{neigh} = [\Sigma_g(R') * \phi(R')](R) \qquad (20)$$

and the total mean density contrast can be written as

$$\Delta\Sigma(R) = \Delta\Sigma_g(R) + \Delta\Sigma_{neigh}(R). \qquad (21)$$

Note that neighboring galaxies do not contribute linearly to the density contrast because they lie at the edge of the aperture. Because fainter galaxies are not counted in our overdensity ϕ, their masses are implicitly assigned to the "mean" mass profile.

To perform the deconvolution of equation 21 and recover the halo density profile, we would need to extrapolate both the overdensity of neighbors and the GMCF to infinity. We instead take a simpler approach, which only requires extrapolating the overdensity. Following Brainerd, Blandford and Smail (1996) and Fischer, et al. (2000), we assume the galaxy profile is represented by a simple model:

$$\rho(r) = \frac{\sigma_v^2 s^2}{\pi G r^2 (r^2 + s^2)} \qquad (22)$$

where σ_v is the central velocity dispersion for $r \ll s$ and s is an outer scale length. For $r \ll s$, this profile resembles an isothermal ($\propto r^{-2}$), and for $r \gg s$ the profile cuts off quickly as r^{-4}. Integrating along the line of sight, we get the projected density profile

$$\Sigma_g(R) = \frac{\sigma_v^2}{2GR} \left(1 - \frac{R}{\sqrt{R^2 + s^2}} \right). \qquad (23)$$

We see that this is the same as the SIS in equation 17 with a cutoff radius s. This model has a finite mass, with $M_{tot} \propto s$.

Taking $\phi(R) = (R/0.94\mathrm{Mpc})^{-0.74}$, we convolve the model density with $\phi(R)$ as in equation 20 and construct the model density contrast as in equation 21. We then perform χ^2 fitting of this model against the data shown in figure 7 to extract the best-fit galaxy parameters σ_v and s.

The top plot in Figure 21 shows the 68%, 95%, and 99% confidence regions for these fits. We have used the full covariance matrix to estimate the χ^2 statistic. As in Fischer, et al. (2000), we can only put a lower limit on the outer scale length, $s \geq 230h^{-1}$ kpc (95% conf.). The velocity dispersion is well constrained, however, to be in the range 100-130 km s^{-1} (95% conf.), with a best-fit value of $\sigma_v = 113$ km s^{-1} ($v_c = 160$ km s^{-1}).

It is worth commenting on the comparison of this result to the results in Fischer, et al. (2000). The size of the lens samples are comparable ($\sim$28,000 there vs. $\sim$31,000 here), and hence the sensitivity to cutoff radius is similar. The difference between these lens samples is that the Fischer, et al. (2000) sample was magnitude selected from r^*=16-18, and this sample is selected(by the standard SDSS spectroscopic survey selection) as all galaxies with $r^* \leq 17.6$. The effect is to focus on a less luminous, and hence less massive, lens sample. In addition, we now know from SDSS spectroscopy that the mean redshift estimated for the Fischer, et al. (2000) lens sample was overestimated by about 35%. Correcting this would reduce the best fit σ_v for that sample by about the same factor. The results here are in agreement with our earlier results. Since they are based on lens samples with spectroscopic redshifts these results are substantially more robust.

The best fit total density contrast and the corresponding central galaxy are overplotted in the top plot of Figure 22. As expected, the density contrast is completely dominated by the central galaxy for small radii, while the contribution from neighbors becomes increasingly important for larger radii. At about 950 h^{-1} kpc the contribution from neighbors dominates. It is worth noting that, although there is on average 1 neighbor within 260 h^{-1} kpc, the aperture used in §5, the net contribution of neighbors to the *density contrast* within that radius is $\lesssim$ 10%. For the average galaxy, the contribution of neighboring galaxies is not a dominant factor in the $M_{260}/L_{central}$ measurements described in §5.

There are in the literature other approaches to extracting the "isolated mean galaxy" from lensing data of this kind. Schneider & Rix (1997) have presented a method in which a model galaxy, with certain luminosity scaling relations, is fit to the entire set of source and lens galaxies. An intellectually similar, but technically quite different approach has been developed by Johnston (2001). While these techniques present an interesting alternative to the more direct measurement of the GMCF, they require knowledge of all lens objects contributing to the shape of each source galaxy. This information is only available for objects far from the edges of the observed region. These SDSS data, taken in long strips, have little area far from the edges. As a result, we will pursue this alternative analysis when a number of contiguous SDSS stripes are available for lensing studies.

5.3. *Tests of galaxy profile determination*

If the deconvolution method described in §5.2 is properly removing the effects of neighbors, we should be able to choose galaxies from different environments, but with the same luminosity, and recover consistent halo parameters. We use the Voronoi tesselation of the galaxy positions described in §4.4 to select samples of galaxies from high and low density regions. The galaxies from high and low density regions have i^* luminosity that is similar to the mean luminosity of the entire lens sample (2.1, 2.0, and $2.0 \times 10^{10} L_{\odot}$ respectively). The overdensity of neighbors for the high and low density samples is measured in the same manner desribed in §5.2. Results are shown in Figure 20. The galaxies selected to have high local density do have a higher ϕ by about a factor of two at every radius,

and the best-fit power law is

$$\phi_{high}(R) = \left(\frac{R}{1.74\mathrm{Mpc}}\right)^{-0.82} \mathrm{Mpc}^{-2}. \qquad (24)$$

For the galaxies selected to have lower local density, we find that the amplitude ϕ_{low} is actually negative, indicating that these galaxies tend to live in underdense regions. We find that ϕ_{low} does not fit well to a power law. We represent it instead as a Gaussian with scale length 400 h^{-1} kpc, and use this to do the deconvolution.

The density contrast measured around these subsamples is shown in Figure 22. Indeed, the signal at large radii flattens out as expected for galaxies in higher density regions, and the signal from underdense regions drops more rapidly to zero.

Repeating the deconvolution analysis of §5.2 on the high density lens sample, we find the confidence regions for σ_v and s shown in the middle plot of figure 21. The allowed values for the velocity dispersion agree quite well with those found for the entire lens sample, 100-135 km s^{-1} (95% conf). We still find only a lower bound on the cutoff radius, $s \geq 260h^{-1}$ kpc (95% conf.). The best-fit model and central galaxy are overplotted on the middle figure 22, demonstrating the large contribution to the density contrast made by the neighboring galaxies.

For the low-density sample, we find that the void-like regions surrounding these galaxies actually *reduces* the lensing signal, and density contrast must be added to the measured signal to reconstruct the central galaxy. Although we cannot constrain the outer scale at all, we find that the best-fit velocity dispersion is still consistent with that inferred for the average galaxy, 75-170 km s^{-1} (95% conf.), with a best-fit value of 125 km s^{-1}.

This test demonstrates that we are able to recover similar halo parameters for galaxies of similar luminosity that come from very different environments. This suggests that we have a reasonable understanding of the effects of bright neighboring galaxies on the density constrast.

6. SUMMARY AND DISCUSSION

Our understanding of structure formation in the universe has evolved substantially over the last thirty years. We no longer expect galaxies to form as discrete, isolated objects. Nor is the formation of a galaxy simply a series of mergers of discrete, otherwise isolated objects. Instead, luminous galaxies are roughly discrete tracers of mass, embedded in a smoothly varying dark matter environment. Over time, the very smooth matter distribution of the early universe becomes more and more inhomogeneous. Despite this, galaxies are today embedded in dark matter halos which overlap to a degree which invalidates discussion of them as discrete objects.

We have presented measurements of a galaxy-mass correlation function and its dependence on a variety of measured galaxy properties. We measured the dependence of the GMCF on galaxy luminosity. While the shape of the GMCF is little affected by luminosity, the amplitude can vary strongly. The GMCF has little relation to u' luminosity, reflecting the fact that much of this luminosity is derived from localized, short lived episodes of star formation. The GMCF is strongly dependent on the luminosity of galaxies in the g', r', i', and z' bands. The luminosity

in these bands is dominated by low mass stars, and hence reflects the integrated star formation history of the galaxy.

We have examined the relationship between the GMCF and the morphology of galaxies. The GMCF is much stronger for elliptical galaxies than it is for spirals. Ellipticals typically reside in halos which are more massive than spirals.

We examined the relationship between GMCF and galaxy environment. We found that the amplitude of the GMCF near the center is very similar for galaxies of the same luminosity drawn from overdense and underdense regions, yet the shape of the GMCF at large radii is quite different. This result confirms the notion that the GMCF in the central regions, out to perhaps 300 h^{-1} kpc, is dominated by mass clearly associated with the central galaxy. The GMCF at large radius, by contrast, is primarily effected by the presence of neighboring objects.

In a straightforward effort to quantify the scaling of the GMCF with central galaxy luminosity ($L_{central}$) we derived aperture masses for various classes of lenses based on fits to the inner 260 h^{-1} kpc of their GMCF (M_{260}). Comparison of M_{260} to the mean $L_{central}$ confirms a linear scaling in the g', r', i', and z' bandpasses. These measurements of M_{260} also allowed us to probe quantitatively the $M_{260}/L_{central}$ relations for spiral and elliptical galaxies. Despite the substantial difference between the GMCF for spirals and ellipticals, there is little difference in the relationship between their GMCF and luminosities in red bands. Since spiral and elliptical galaxies occupy substantially different average local environments, the consistency of these GMCF/luminosity relations reinforces the notion that the GMCF measured within 260 h^{-1} kpc is primarily associated with the central object.

It is worth noting that many efforts to understand the relation between galaxy mass and light have utilized measurements of blue light (intermediate between the SDSS u' and g' bands). Our results suggest that any such attempt is problematic. They cast doubt on attempts to explain the Tully-Fisher relation in B-band with the assumption that rotational velocity is a constant fraction of circular velocity at virial radius (Mo, Mao & White 1998). In the red bands the situation is significantly simpler, and our data are consistent with the assumption that light traces mass on halo scales, independent of luminosity and morphological type. Future studies of galaxy mass and its relation to luminosity should concentrate on luminosities measured in red bands.

Finally, we made an effort to understand the effect of galaxy clustering on naive interpretations of these measurements. By deconvolving the GMCF and the lens-lens correlation function we obtain rough estimates of the relative contributions of lens galaxies and comparably luminous neighbors. At the 260 h^{-1} kpc radius of our $M_{260}/L_{central}$ measurements we estimate that the contamination from neighbors is typically 10%. No evidence for a cutoff in the deconvolved GMCF is seen. We place 95% confidence limits on such a cutoff at 230 h^{-1} kpc within the context of SIS models. Current data are not sufficiently accurate to distinguish between SIS and NFW profiles and the latter also provide a good fit to the data.

It appears that the integrated star formation history of a galaxy (as reflected in its i' luminosity for example) is closely correlated with the depth of the dark matter halo in which the galaxy formed. This statement seems to be true independent of the luminosity or morphology of the galaxy. Two factors are required for this correlation to hold. First, the fraction of baryonic to total mass on halo scales must be roughly constant. If this baryon fraction is constant, the amount of material available to form stars will be related to the halo mass. That the baryon fraction should be roughly constant is not too surprising, as the regions from which these halos are drawn are quite large. Altering the baryon fraction substantially on these scales would require a mechanism for either separating baryons from dark matter before halo potentials form, or for moving baryons from one potential well to another.

The second requirement for a close relation between mass and luminosity is a roughly constant efficiency for star formation in galaxies of different sizes. This efficiency is clearly not constant when measured on short timescales. This is why the GMCF is so weakly related to the u' luminosity of galaxies. The luminosity of galaxies in the red bands, however, reflects the integrated star formation history of the galaxies. The direct relation between the GMCF and these red luminosities suggests that this integrated star formation efficiency is, in fact, relatively constant across a range of galaxies.

These measurements are the first of many which can be made with existing and future SDSS data. They provide a direct comparison between the luminous properties of objects and the projected surface density of the dark matter environment in which they reside. These weak lensing measurements are particularly powerful for their ability to provide a consistent approach to the study of objects with a wide range of properties. They can be used in an identical way with galaxies of all types, luminosities, and environments.

7. FUTURE PROSPECTS

While the studies presented here go substantially beyond previous galaxy-galaxy lensing studies, they represent only the beginning of what can be done with SDSS data. All the studies described here are based on SDSS commissioning data which does not meet survey data quality requirements. The survey data now being taken have substantially better image quality and PSF stability. The improved image data allow us to better measure galaxy shapes and to include more galaxies in our source catalog. More important, the data presented here are drawn from only about 4% of the final SDSS survey area. The full data set will allow repetition of all these measurements with more than 5 times the signal to noise.

The enhanced statistical power provided by the full SDSS can be used in an alternative way as well. We can divide the universe of galaxies into as many as twenty-five subsets, and obtain for each a GMCF with S/N comparable to those presented here. This will allow us to study scaling relations between the GMCF and a wide range of galaxy properties; including scale length, local environment, evidence of recent mergers, stellar population and age estimates, etc.

Additional analysis of galaxy halo concentrations is possible. SDSS spectra are of sufficiently high quality to provide measured velocity dispersions for essentially every

early type galaxy (Bernardi, et al. 2001). Typical errors in σ_v are <15 km/s. These velocity dispersions provide a dynamical measure of the mass in the central $\sim 10\ h^{-1}$ kpc of these galaxies. Comparison of these measurements to the GMCF measurements on $250\ h^{-1}$ kpc scales will provide a direct probe of variations in the concentration of galaxy halos. This analysis is underway now, using a sample of more than 10,000 early type galaxies with measured σ_v.

As mentioned above, there are other analysis techniques which can be applied to this data (Schneider & Rix 1997; Johnston 2001). They will be much more effective when the SDSS has completed imaging and spectroscopy of a region with a less extreme axis ratio.

A very important project will be direct comparison of these results to measurements conducted in the same manner in the results of N-body simulations. Some initial work based on the GIF (Kauffmann, Colberg, Diaferio, & White 1999) semianalytic simulations has been done by Guzik & Seljak (2001) and Stebbins (2001). Another promising approach is to use halo models to quantify galaxy-galaxy lensing (Seljak 2000). The ultimate outcome of such analyses will be the galaxy luminosity function as a function of halo mass. We expect to substantially expand this work in the future, providing essential feedback to the models of galaxy formation.

Extension of this approach to studies of other kinds of 'objects' is also possible. In addition to the galaxy-mass correlation function described here, we can measure the group-mass correlation function, the cluster mass correlation function, even a void-mass correlation function. All that is required is an input catalog of object locations and redshifts. A simple example demonstrating our ability to measure the cluster-mass correlation function appeared in Sheldon, et al. (2001).

Weak lensing within the SDSS provides a powerful new tool for probing the relationship between luminous objects and the dark matter environment in which they reside. This is particularly timely as we enter an era of precision cosmology, in which the cosmological parameters are well constrained, and these details of galaxy bias can no longer be ignored. SDSS lensing measurements provide strong constraints on the total correlation between objects and mass, and hence provide simple, direct constraints to N-body simulation results.

REFERENCES

Abraham, R. G., Valdes,F., Yee, H. K. C., van den Bergh, S., 1994, ApJ, 432, 75
Bahcall, N., Cen, R., Dave, R., Ostriker, J.P., and Yu, Q., astro-ph/0002310
Barnes, J. E. 1999, ASP Conf. Ser. 182: Galaxy Dynamics - A Rutgers Symposium, 463
Baugh, C. M. and Efstathiou, G. 1993, MNRAS, 265, 145
Bernardi, M., et al., 2001, personnal communication
Bernstein, G., et al., 2001, in preparation
Bershady, M. A., Jangren, A., & Conselice, C. J. 2000, AJ, 119, 2645
Blandford, R. D., Saust, A. B., Brainerd, T. G. and Villumsen, J. V. 1991, MNRAS, 251, 600
Blanton, M. R. et al. 2001, AJ, 121, 2358
Brainerd, T. G., Blandford, R. D. and Smail, I. 1996, ApJ, 466, 623
Burkert, A. & Naab, T. 2000, American Astronomical Society Meeting, 197, 5605
Carlberg, R. G., Yee, H. K. C., & Ellingson, E. 1997, ApJ, 478, 462
Evrard, A. E., Metzler, C. A., & Navarro, J. F. 1996, ApJ, 469, 494
Fischer, P., et al., 2000, AJ, 120, 1198
Frieman, J., et al., 2001, in preparation
Fukugita, M., Shimasaku, K., and Ichikawa, T., 1995, PASP, 107, 945
Fukugita, M., et al., 1996, AJ, 111, 1748
Girardi, M. & Giuricin, G. 2000, ApJ, 540, 45
Gunn, J. E., et al., 1998, AJ, 116, 3040
Guzik, J., & Seljak, U., 2001, MNRAS, 321, 439
Hoekstra, H., et al., 2001, ApJ, L5, 548.
Hogg, D., 1999, astro-ph/9905116
Hradecky, V., Jones, C., Donnelly, R. H., Djorgovski, S. G., Gal, R. R., & Odewahn, S. C. 2000, ApJ, 543, 521
Icke, V., & van de Weygaert, R., 1987, å, 184, 16
Kaiser, N., ApJ, 439, L1
Kaiser, N., Squires, G., and Broadhurst, T., 1995, ApJ, 503, 531
Kauffmann, G., Colberg, J. M., Diaferio, A., & White, S. D. M. 1999, MNRAS, 303, 188

Kochanek, C.S., 1996, ApJ, 457, 228
Johnston, D., 2001, personal communication
Lilly, S., J., et al. 1995, ApJ, 455, 50
Ling, E.N., 1987, Ph.D. Thesis, Sussex University, Brighton (England)
Lupton, R., et al., 2001, in preparation
Lynds, R., & Petrosian, V., 1986, BAAS, 18, 1014
Miralda-Escudé, J. 1991, ApJ, 370, 1
Mo, H. J., Mao, S., & White, S. D. M. 1998, MNRAS, 295, 319
Navarro, J. 2001, astro-ph/0012334
Navarro, J. F., Frenk, C. S., & White, S. D. M. 1997, ApJ, 490, 493
Ostriker, J. P., Peebles, P. J. E., & Yahil, A. 1974, ApJ, 193, L1
Petrosian, V. 1976, ApJ, 209, L1
Pier J. R. et al. 2001, in preparation
Sackett, P.D. 1995, IAU Symposium 173, "Gravitational Lensing," Melbourne, July 1995, eds. C. Kochanek and J. Hewitt
Schlegel, D. J., Finkbeiner, D. P., and Davis, M., 1998, ApJ, 500, 525
Schneider, P. & Rix, H. 1997, ApJ, 474, 25
Scranton, et al., in preparation
Seljak, U., 2000, MNRAS318, 203
Sheldon, E., et al., 2001, to appear in ApJ, also astroph/0103029
Shimasaku, K., Fukugita, M., Okamura, S., et al., 2001, submitted for publication in AJ
Siegmund, W., et al., 2001, in preparation
Smith, D., Bernstein, G., Fischer, P., & Jarvis, M., 2001, ApJ, 551, 643
Stebbins, A., 2001, personal communication
Strateva, Iskra. et al., 2001, submitted for publication in AJ
Strauss, M., et al., in preparation
Tucker, D., et al. 2001, in preparation
Tyson, J. A., Valdes, F., Jarvis, J. F. and Mills, A. P. 1984, ApJ, 281, L59
Tyson, J. A. 1985, Nature, 316, 799
Tyson, J. A., Wenk, R. A., & Valdes, F. 1990, ApJ, 349, L1
Uomoto, A., et al., 2000, in preparation

Walsh, D., Carswell, R. F., & Weymann, R. J. 1979, Nature, 279, 381

Webster, R. L. 1985, MNRAS, 213, 871

Wilson, G., Kaiser, N., & Luppino, G., 2000, astro-ph/0008504

Willick, J., 2000, Proceedings of the XXXVth Rencontres de Moriond: Energy Densities in the Universe, astro-ph/0003232

York, D. G. et al. 2000, AJ, 120, 157

Zaritsky, D., Smith, R., Frenk, C. & White, S. D. M., 1997, ApJ, 478, 39

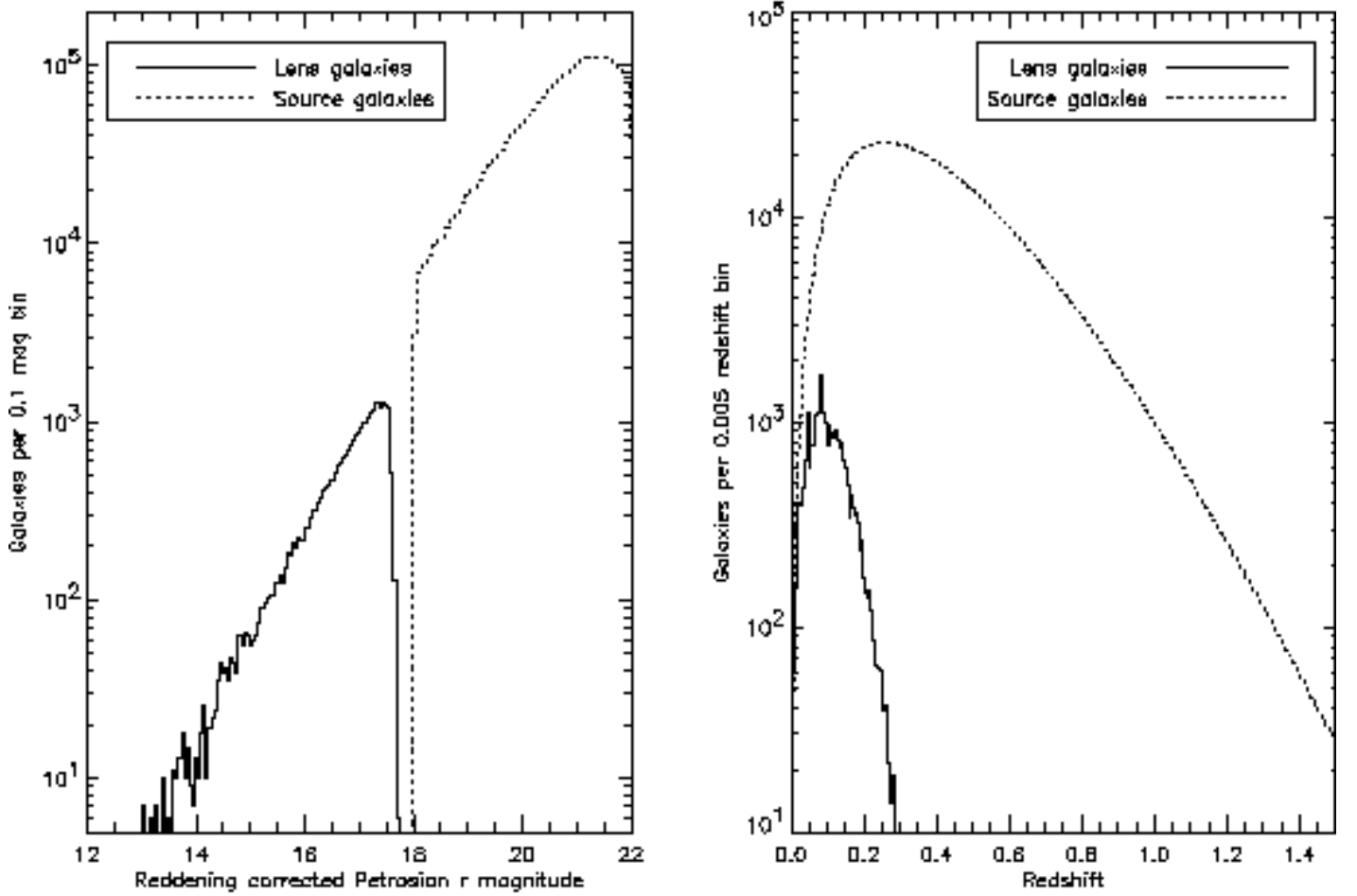Zaritsky, D. 1999, ASP Conf. Ser. 165: The Third Stromlo Symposium: The Galactic Halo, 34

FIG. 1.— Reddening corrected r^* magnitude distribution in bins of 0.1 mag (left) and redshift distribution in bins of .005 (right) for the lens and source galaxies used in this study. The redshift distribution for the source galaxies is estimated by the methods described in §3.3. The source galaxy magnitude distribution is higher than one might expect by extrapolation of the lens distribution because we we require completed SDSS spectroscopy to include a galaxy in the lens sample.
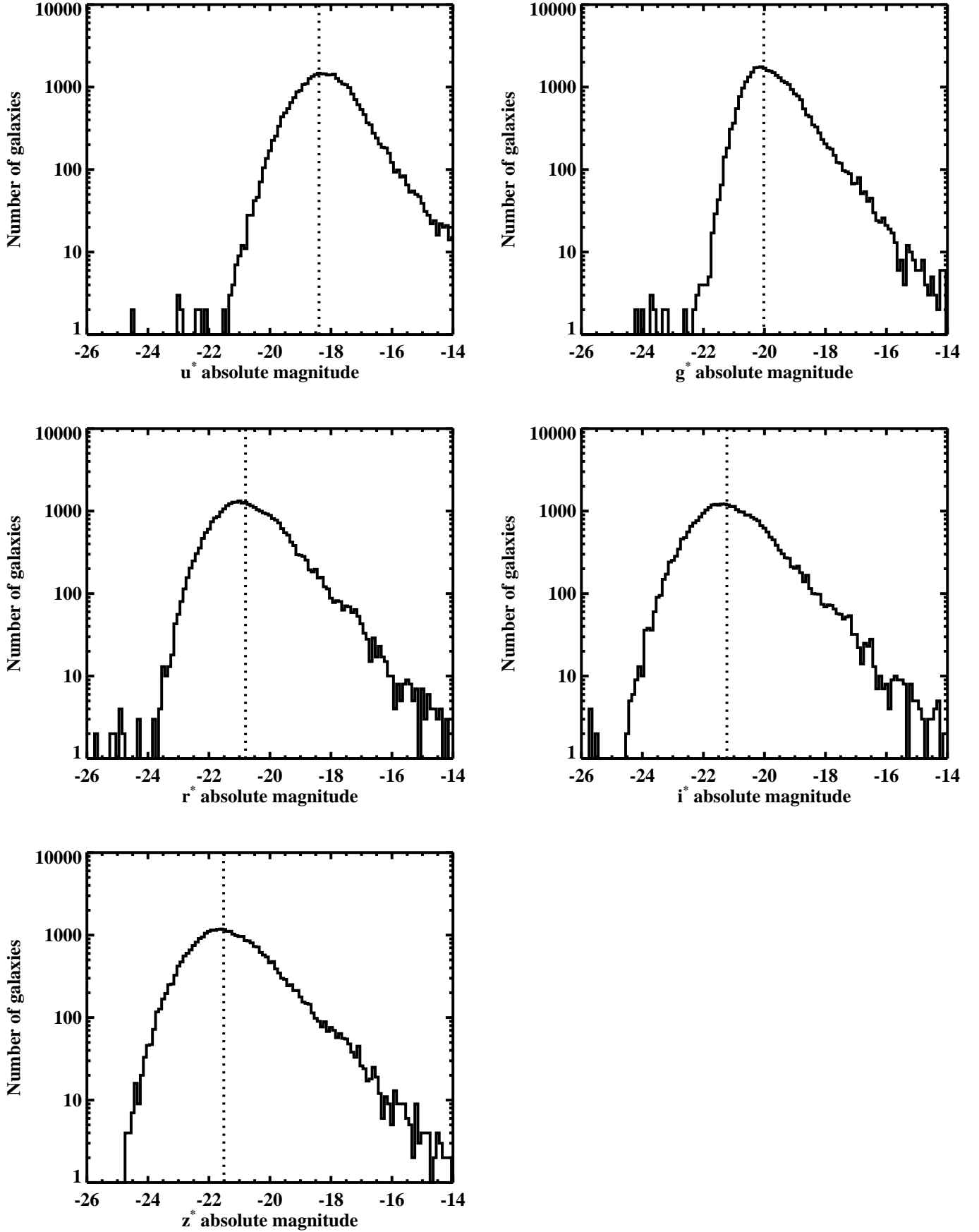
FIG. 2.— The absolute magnitude distributions for the 34,693 lens objects are shown above. Magnitude bins are 0.1 magnitude. The dashed lines mark the values of M* found in each band in Blanton et al. (2001).
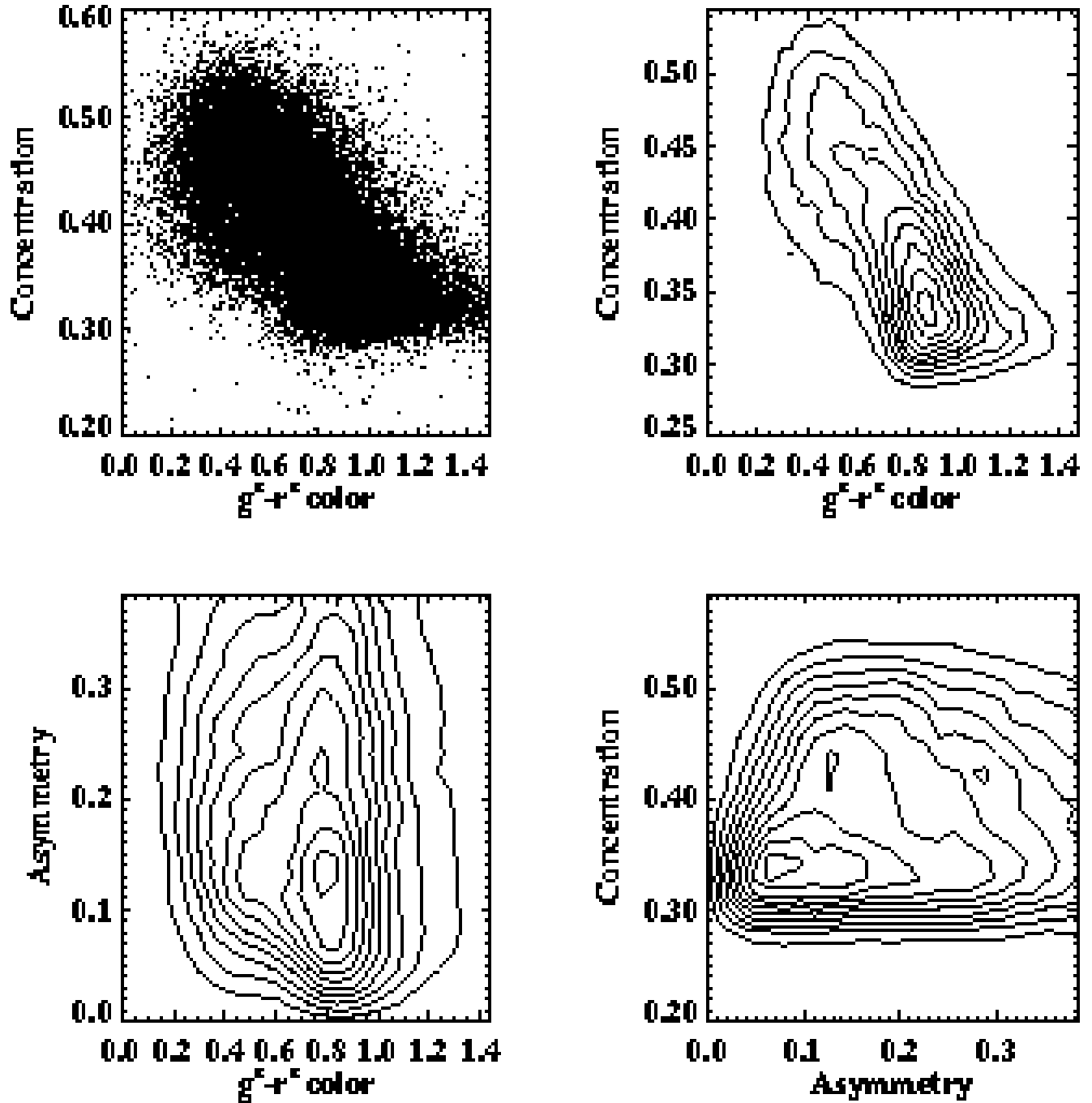
FIG. 3.— This figure demonstrates the correlations among the three classification parameters described in §2.3. On the upper left is a scatter plot of the concentration vs. g^*-r^* color. This is included to give an idea of the scatter of the points. The upper right shows a contour plot of the distribution of galaxies in the concentration vs. g^*-r^* color plane. The lower left shows the relation between asymmetry and g^*-r^* color, and the lower right the relation between concentration and asymmetry.
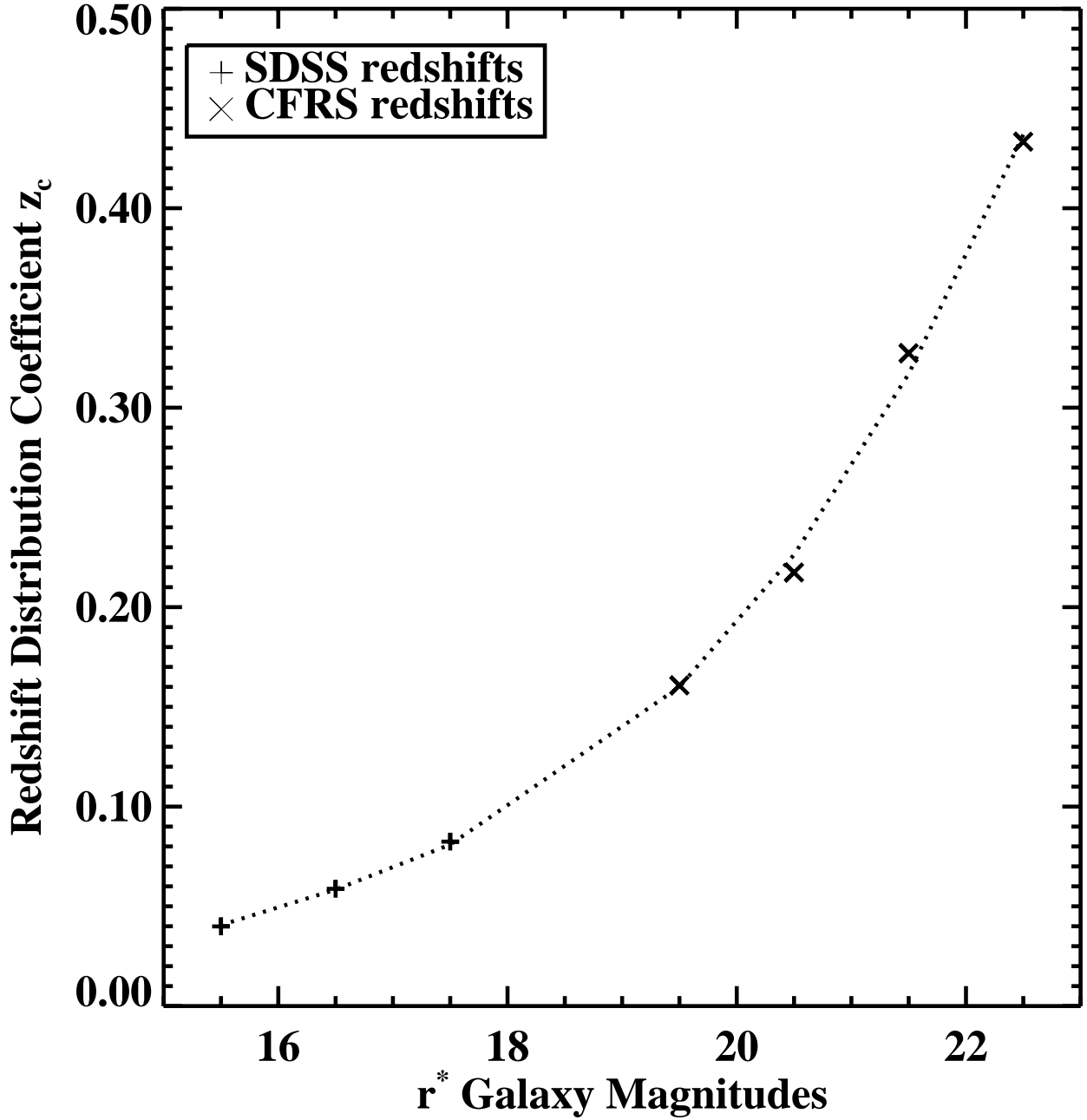
FIG. 4.— This figure shows the relationship between the parameter z_c, which characterizes the redshift distribution of galaxies, and r^* magnitude. Points marked + represent magnitude bins for which z_c was determined from SDSS galaxies. Points marked x represent magnitude bins for which z_c was determined from CFRS galaxies. The dashed line shows the best fit z_c vs. magnitude relation used in determining the source redshift distribution.
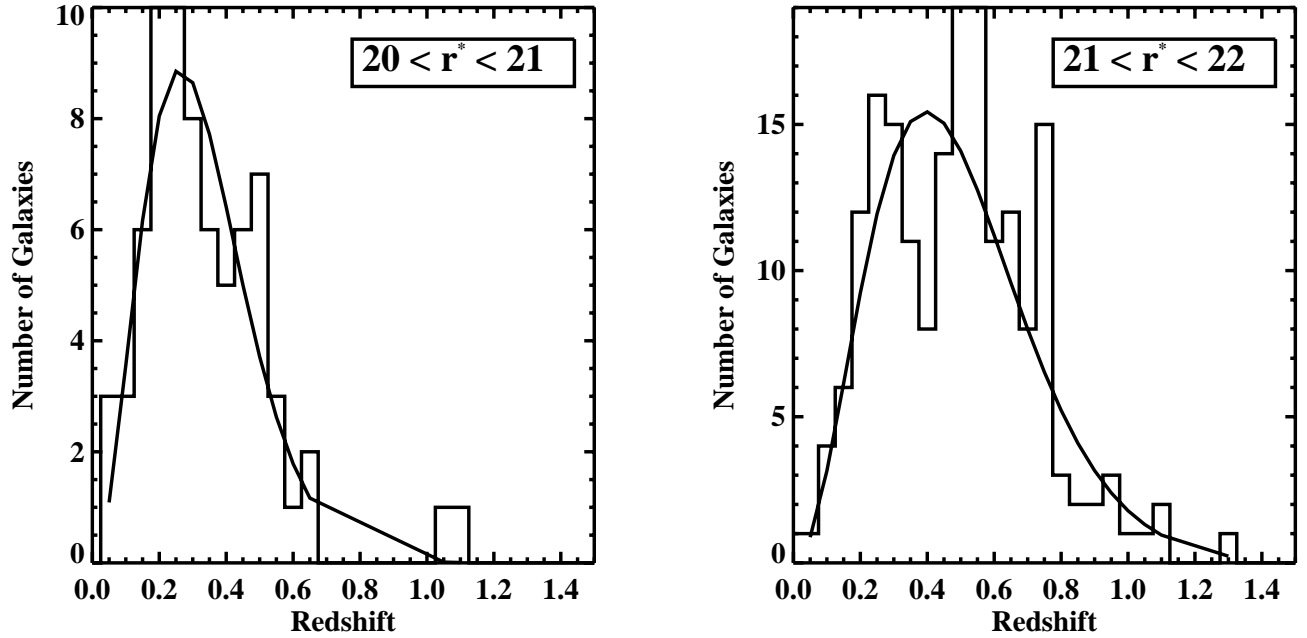
FIG. 5.— The accuracy of source redshift estimation is suggested by this comparison between the real CFRS spectroscopic redshift distribution (histogram) and the redshift distribution estimated by the method described in §3.3 (solid line). The comparison is made for galaxies with $20 < r^* < 21$ on the left, and for galaxies with $21 < r^* < 22$ on the right.
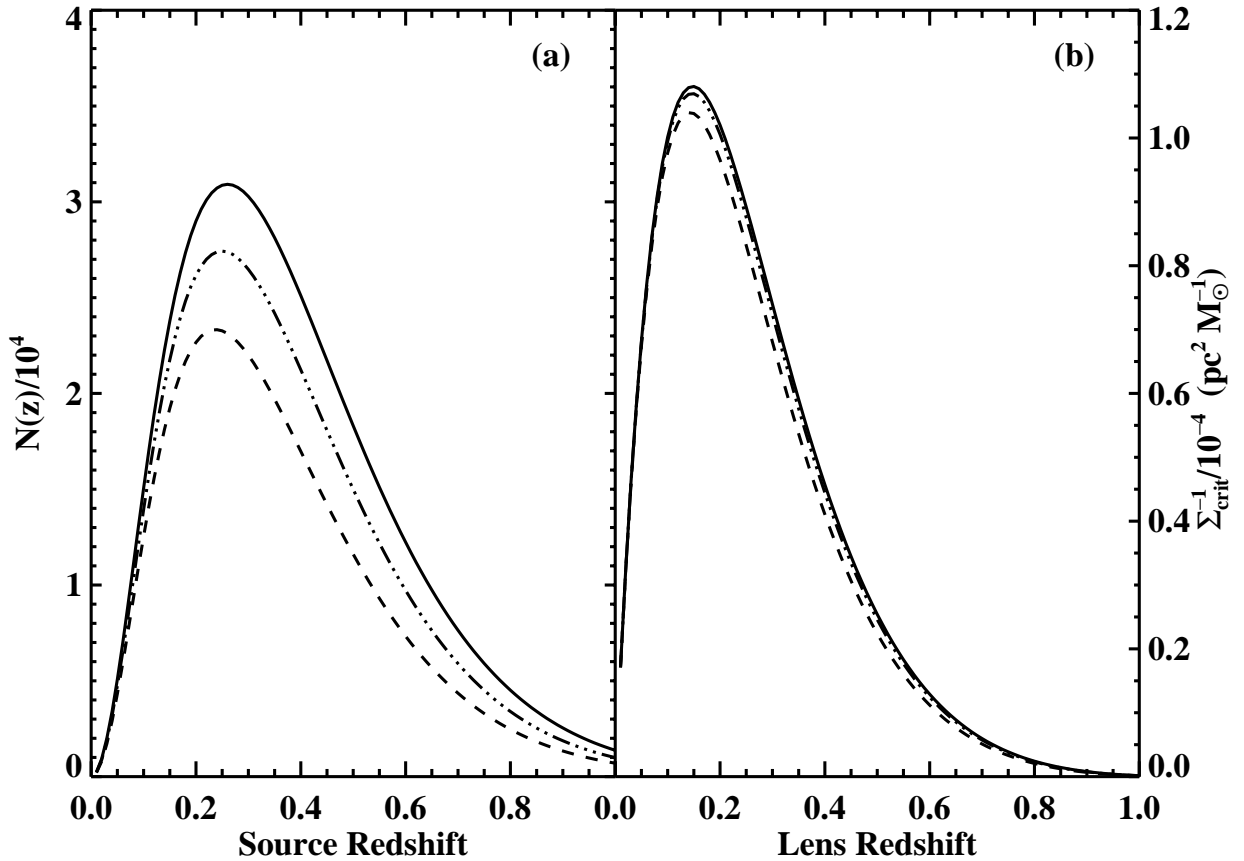
FIG. 6.— Estimated source galaxy redshift distribution in bins of .01 (a) and inferred lensing strength Σ_{crit}^{-1} as a function of lens redshift (b). Source galaxies are taken from the g' (dashed line), r' (solid), and i' (dot-dashed) images.
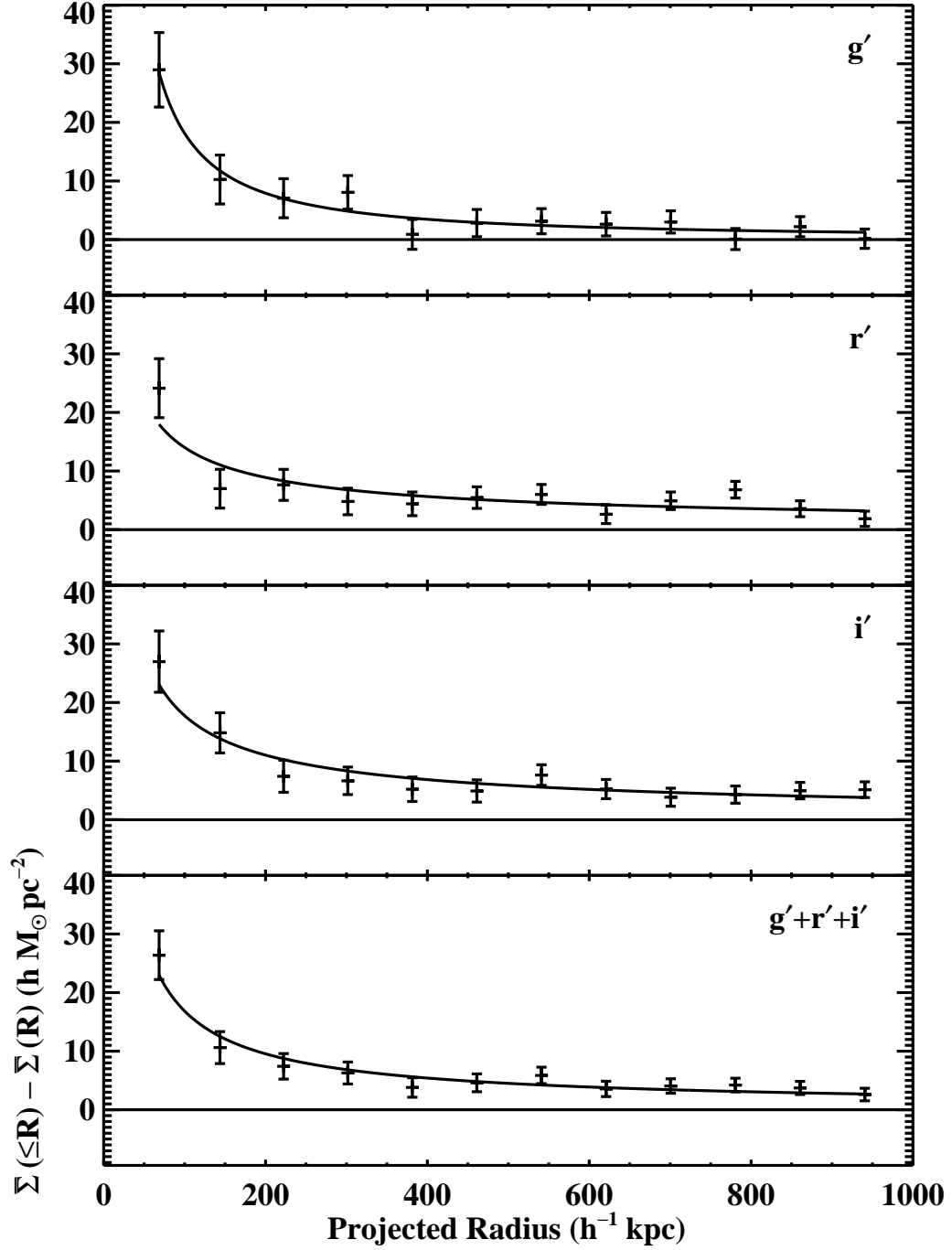
FIG. 7.— Mean density contrast measured as a function of projected radius around ∼31,000 SDSS lens galaxies. The plots are the mean density contrast in g', r', and i' images from the top, with the combined data on bottom. The solid lines are the best-fitting power laws.
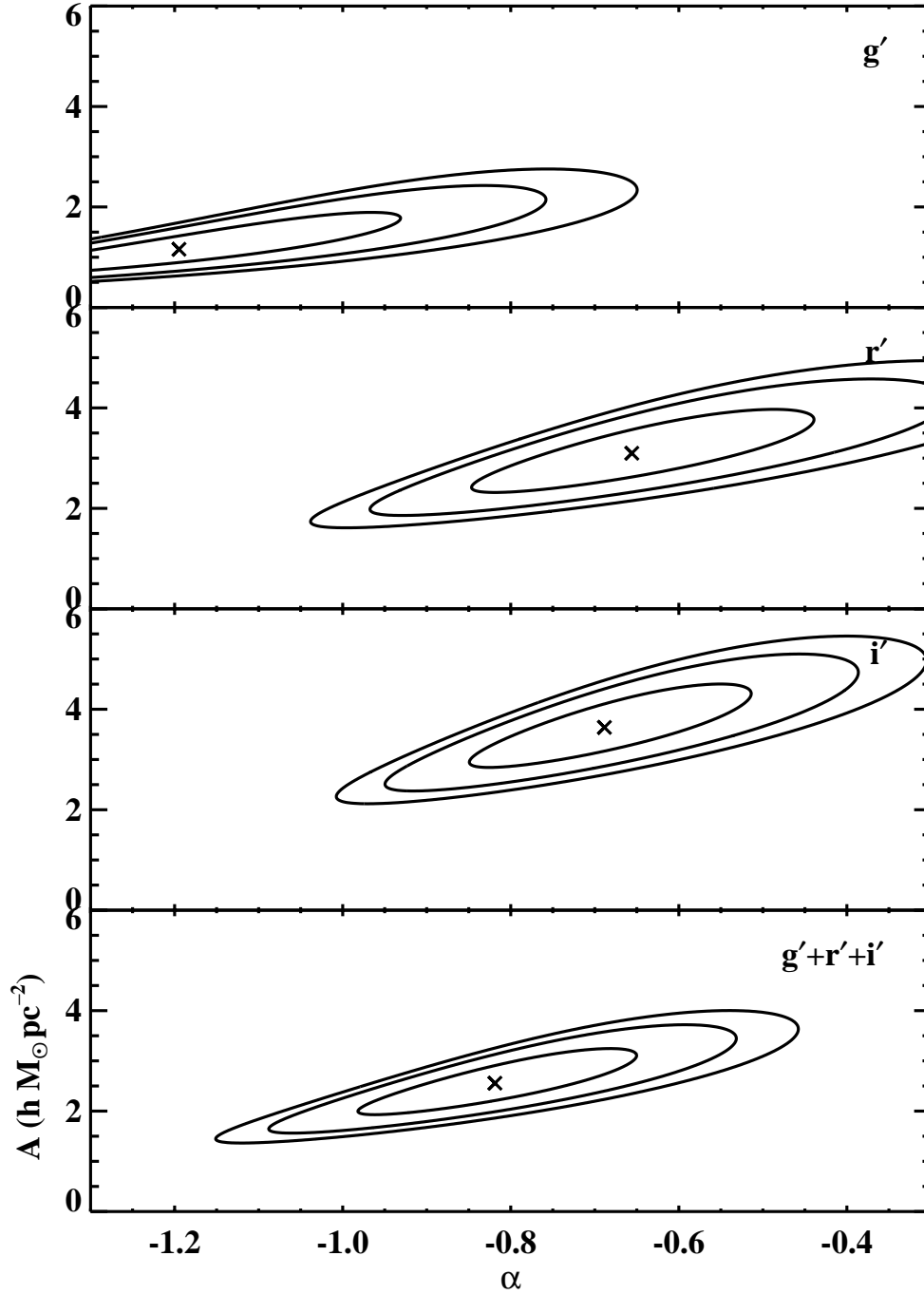
FIG. 8.— Best fits of the GMCF to the function $\Delta\Sigma_+ = A(R/1 \text{ Mpc})^{-\alpha}$ are shown for each band and for the combined data. χ^2 contours for each represent 68%, 95% and 99% confidence.
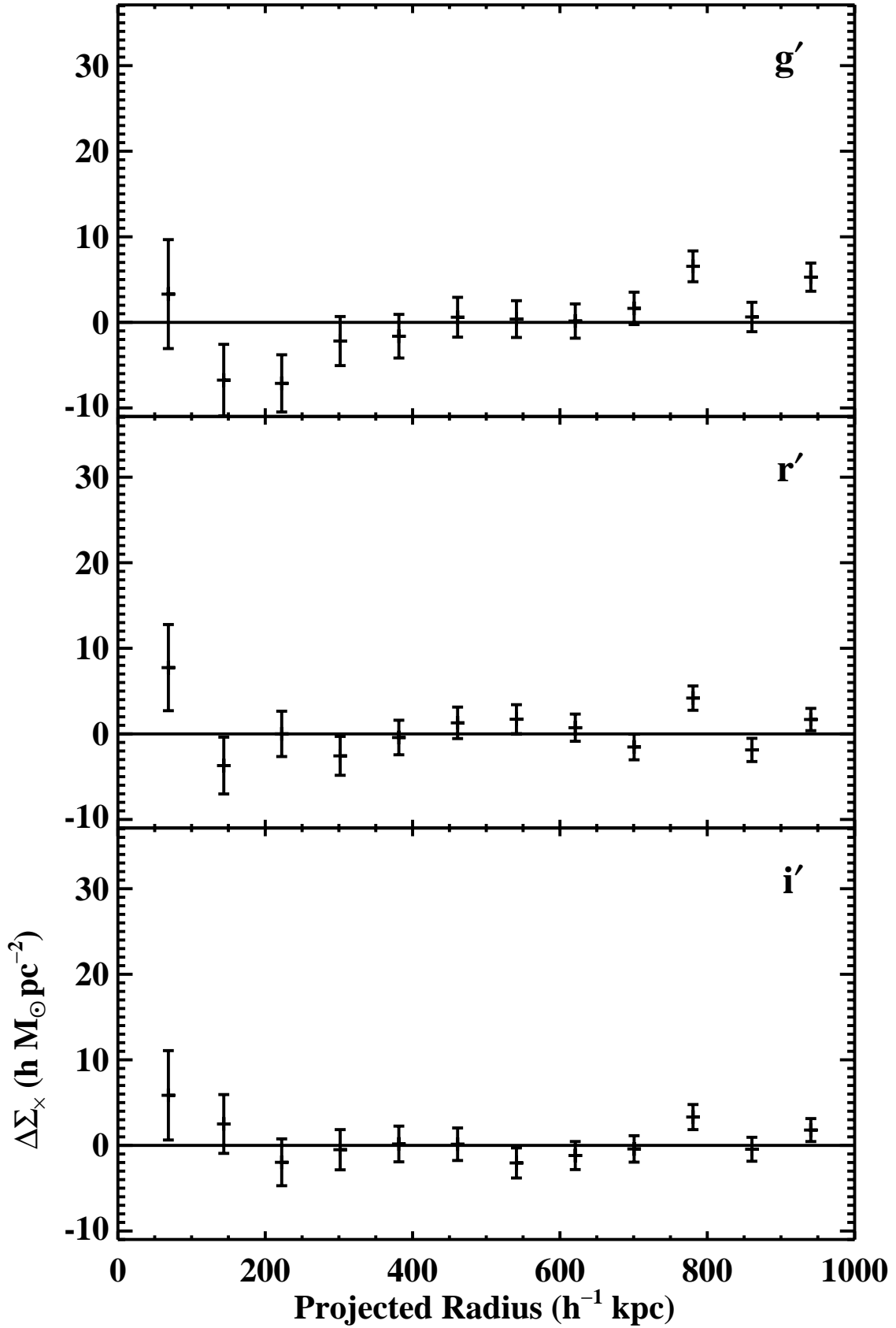
FIG. 9.— The GMCF is measured here around the same SDSS lenses as in Figure 7, but source galaxies have been rotated by 45°. This rotation eliminates the lensing signal observed in Figure 7.

McKay et al.
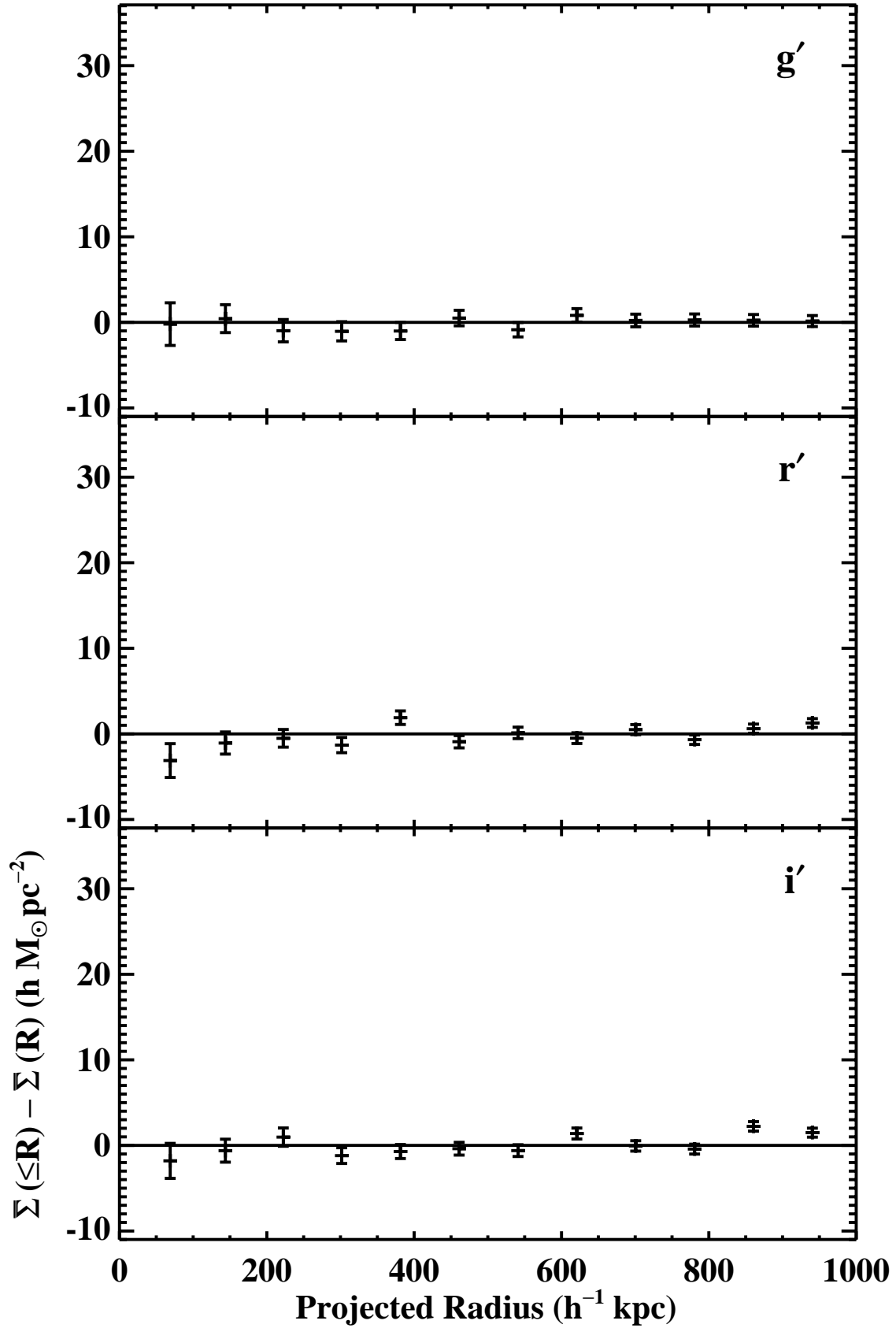
FIG. 10.— The GMCF is measured here around 150,000 random points. Consistency with zero surface mass density contrast around these points confirms that the signal observed in Figure 7 is associated with galaxies.
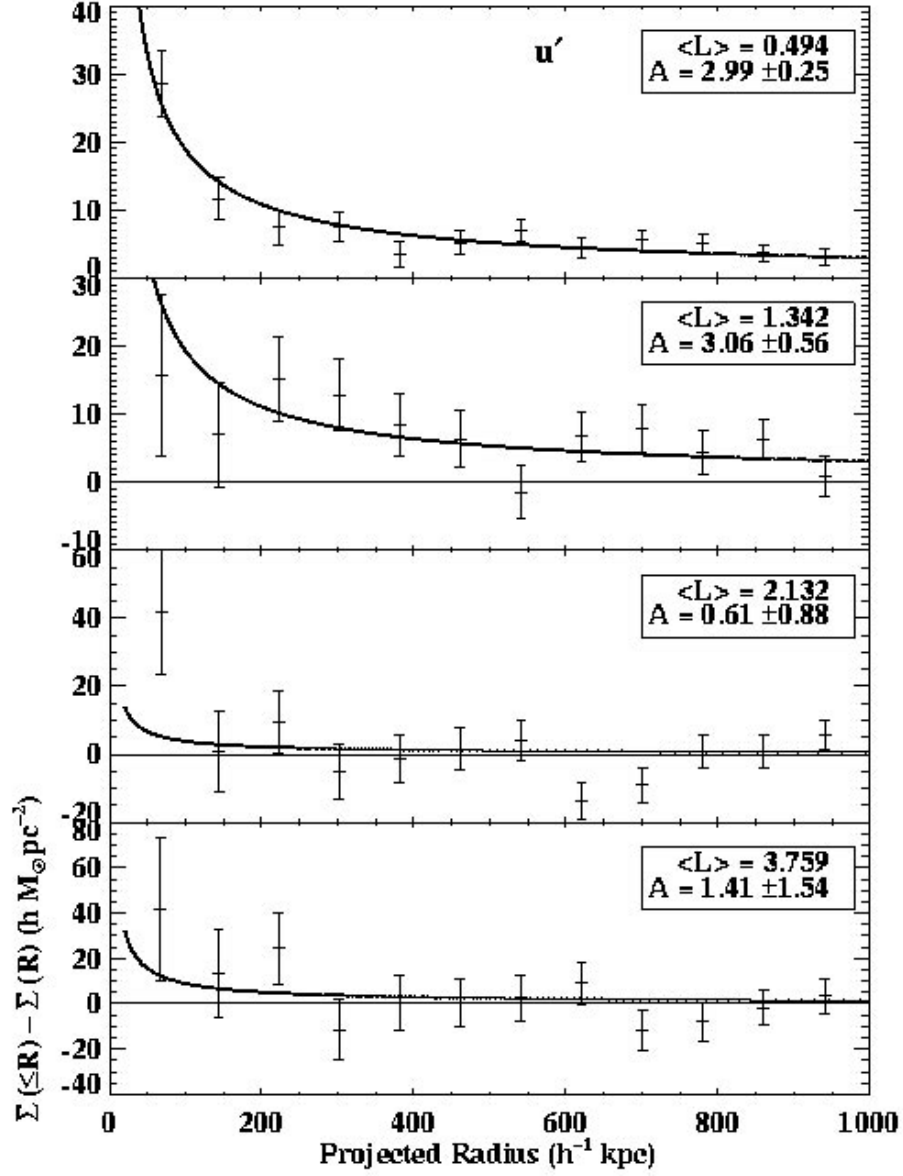
FIG. 11.— GMCF in bins of u^* luminosity. Lines are the best fits to $R^{-0.8}$ power law models corresponding to the noted values of the normalization A. Note that each plot has a different y-axis scale.
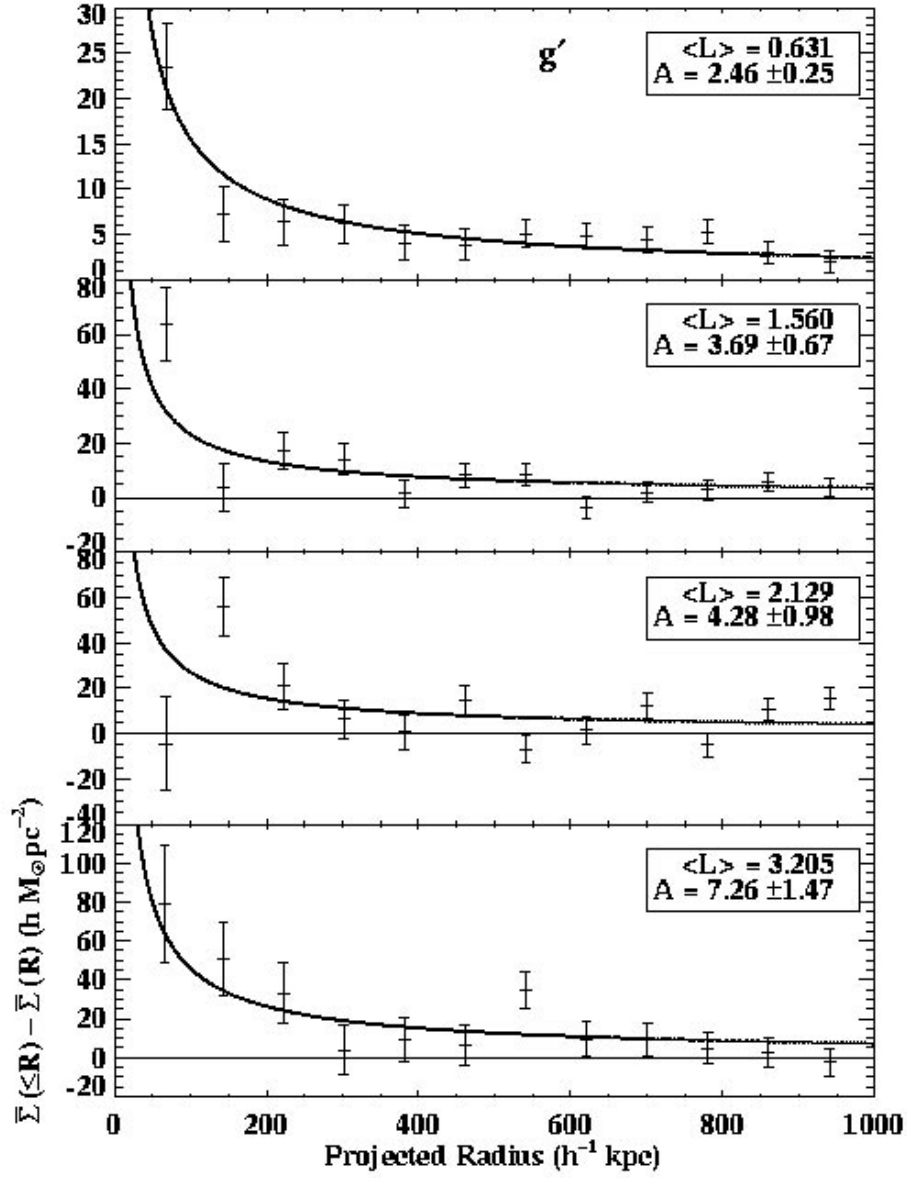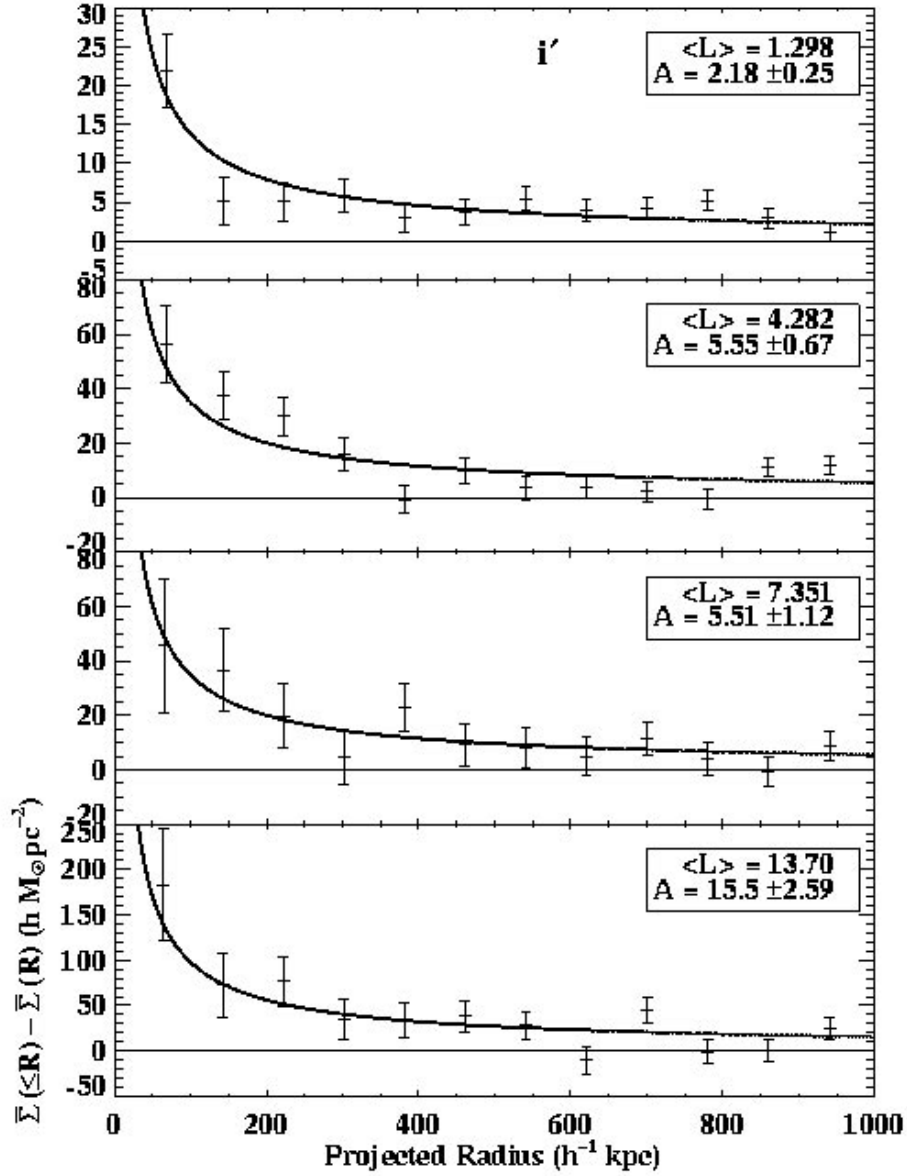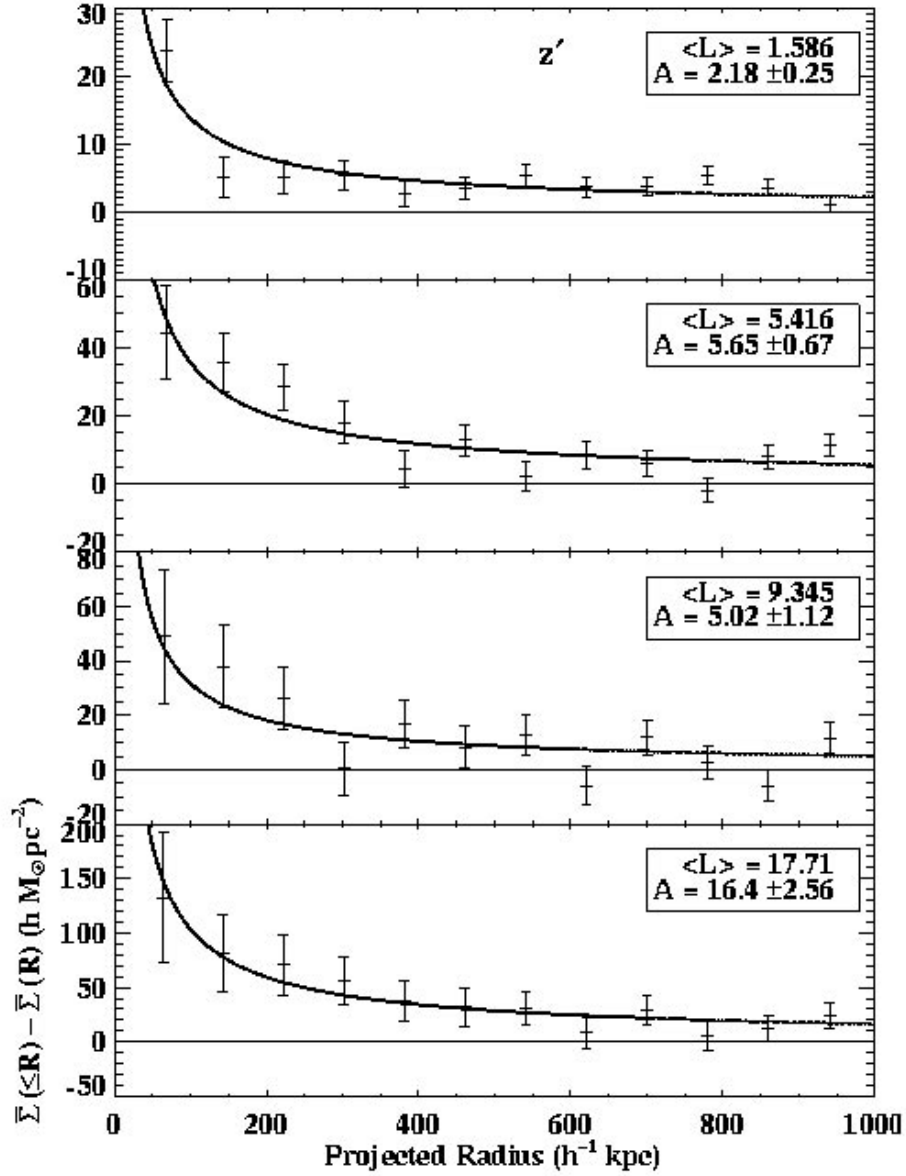
FIG. 12.— GMCF in bins of g^* luminosity. Lines are the best fits to $R^{-0.8}$ power law models corresponding to the noted values of the normalization A. Note that each plot has a different y-axis scale.
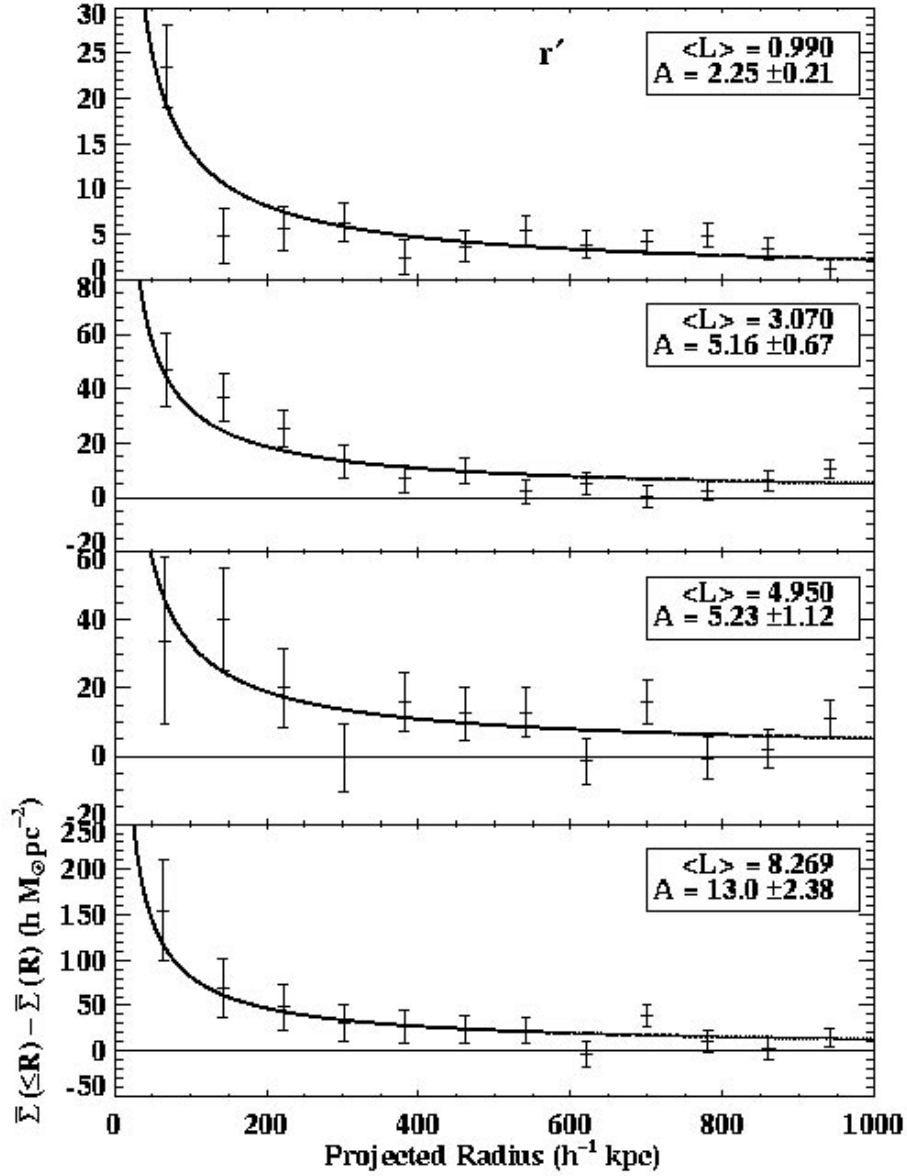
FIG. 13.— GMCF in bins of r^* luminosity. Lines are the best fits to $R^{-0.8}$ power law models corresponding to the noted values of the normalization A. Note that each plot has a different y-axis scale.

FIG. 14.— GMCF in bins of i^* luminosity. Lines are the best fits to $R^{-0.8}$ power law models corresponding to the noted values of the normalization A. Note that each plot has a different y-axis scale.

FIG. 15.— GMCF in bins of z^* luminosity. Lines are the best fits to $R^{-0.8}$ power law models corresponding to the noted values of the normalization A. Note that each plot has a different y-axis scale.

McKay et al.
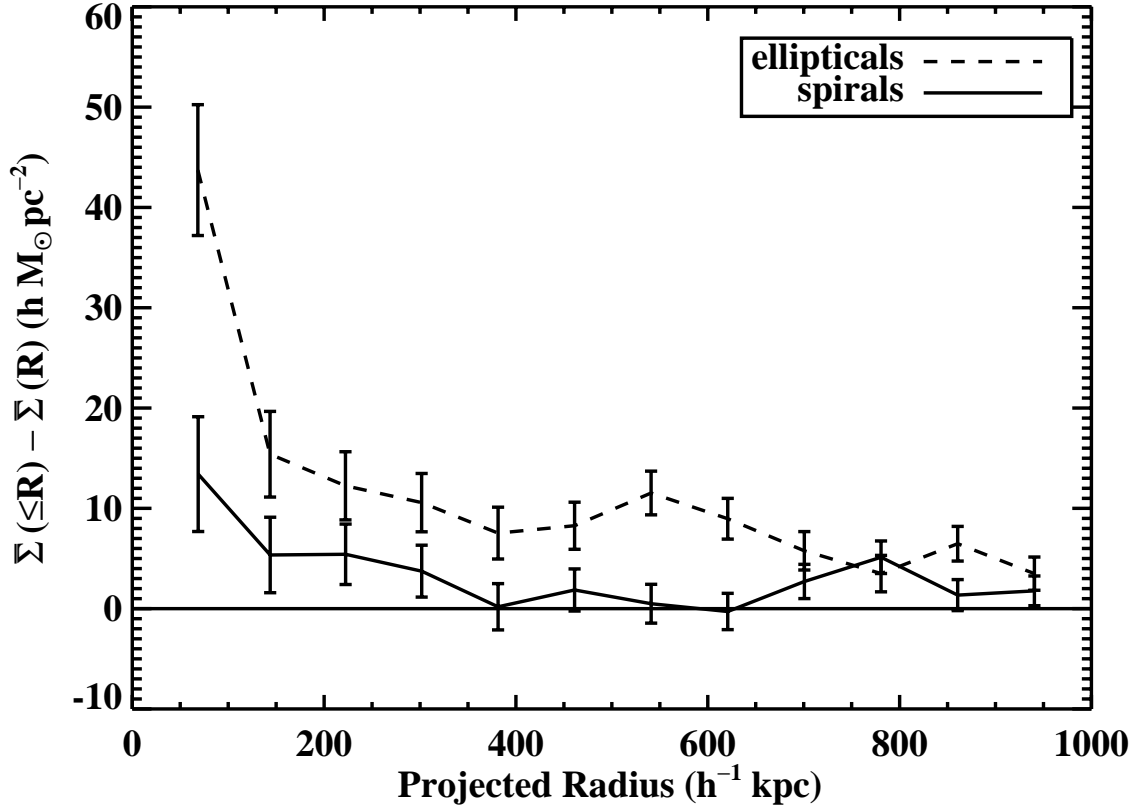
FIG. 16.— This figure compares the GMCF measured around spiral and elliptical galaxies. Sample selection is described in §2.3.
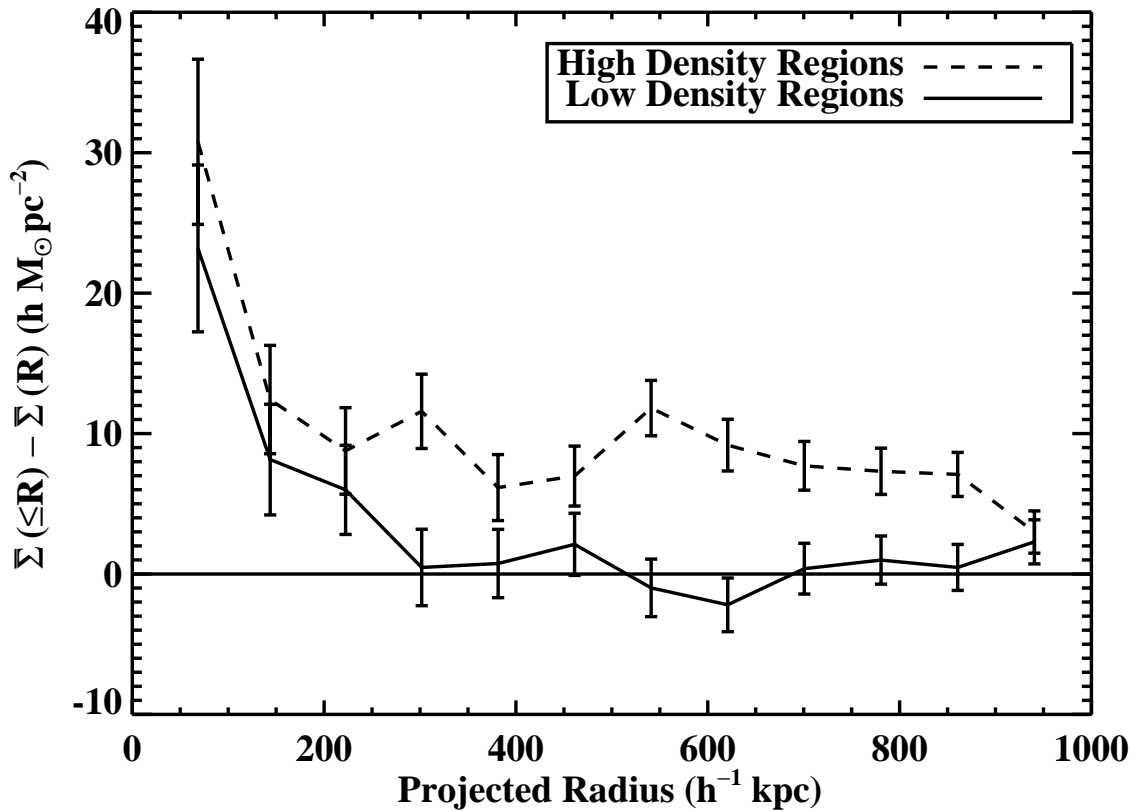

FIG. 17.— This figure compares the GMCF measured around galaxies in high and low density regions. Sample selection is described in §4.4.
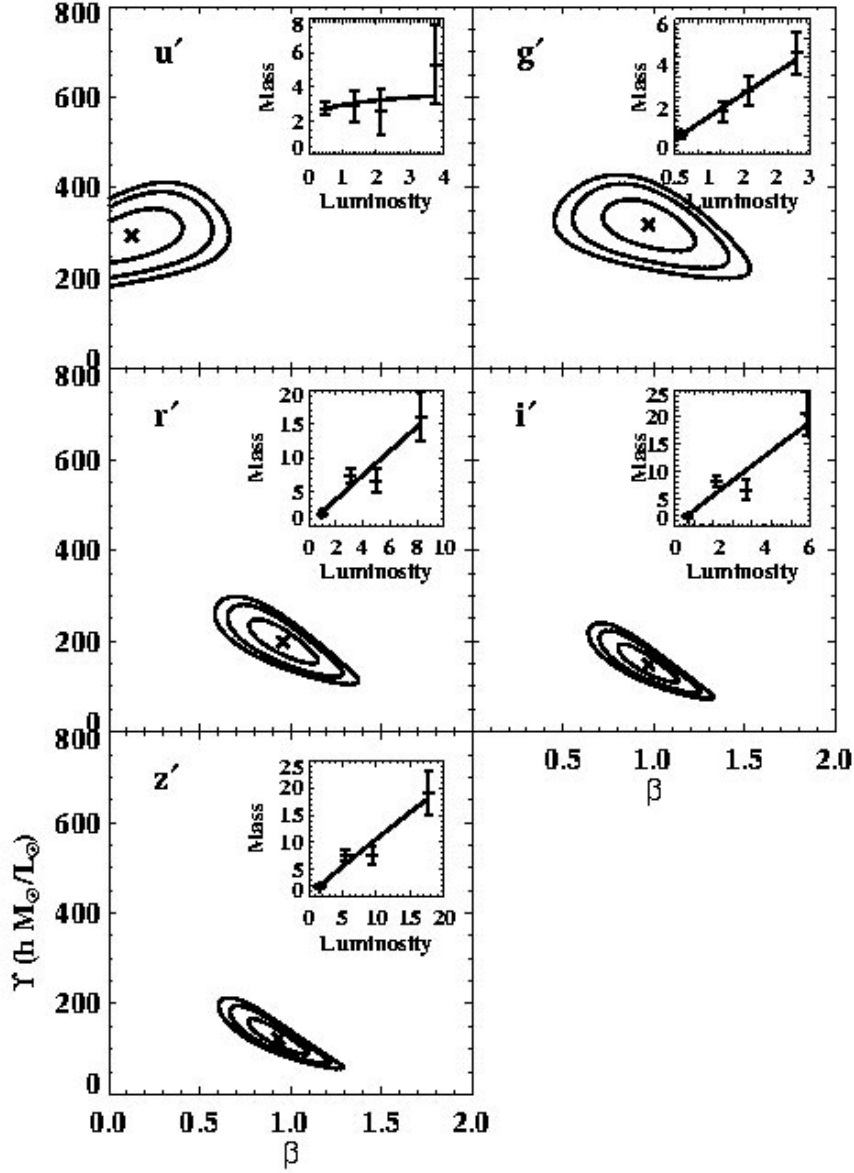
FIG. 18.— The five panels in this figure summarize the relation between M_{260} and luminosity in each of the five SDSS bands. For each band the small inset figure shows this directly. Points in these inset figures are the measured M_{260} and mean luminosity of galaxies in four luminosity bins. The line in these inset figures shows the best fit to a power law relation between M_{260} and luminosity of the form: $M_{260} = \Upsilon \times \left(L_{central}/10^{10}L_\odot\right)^\beta$. The larger figure shows 68%, 95%, and 99% confidence contours for the fit parameters Υ and β.
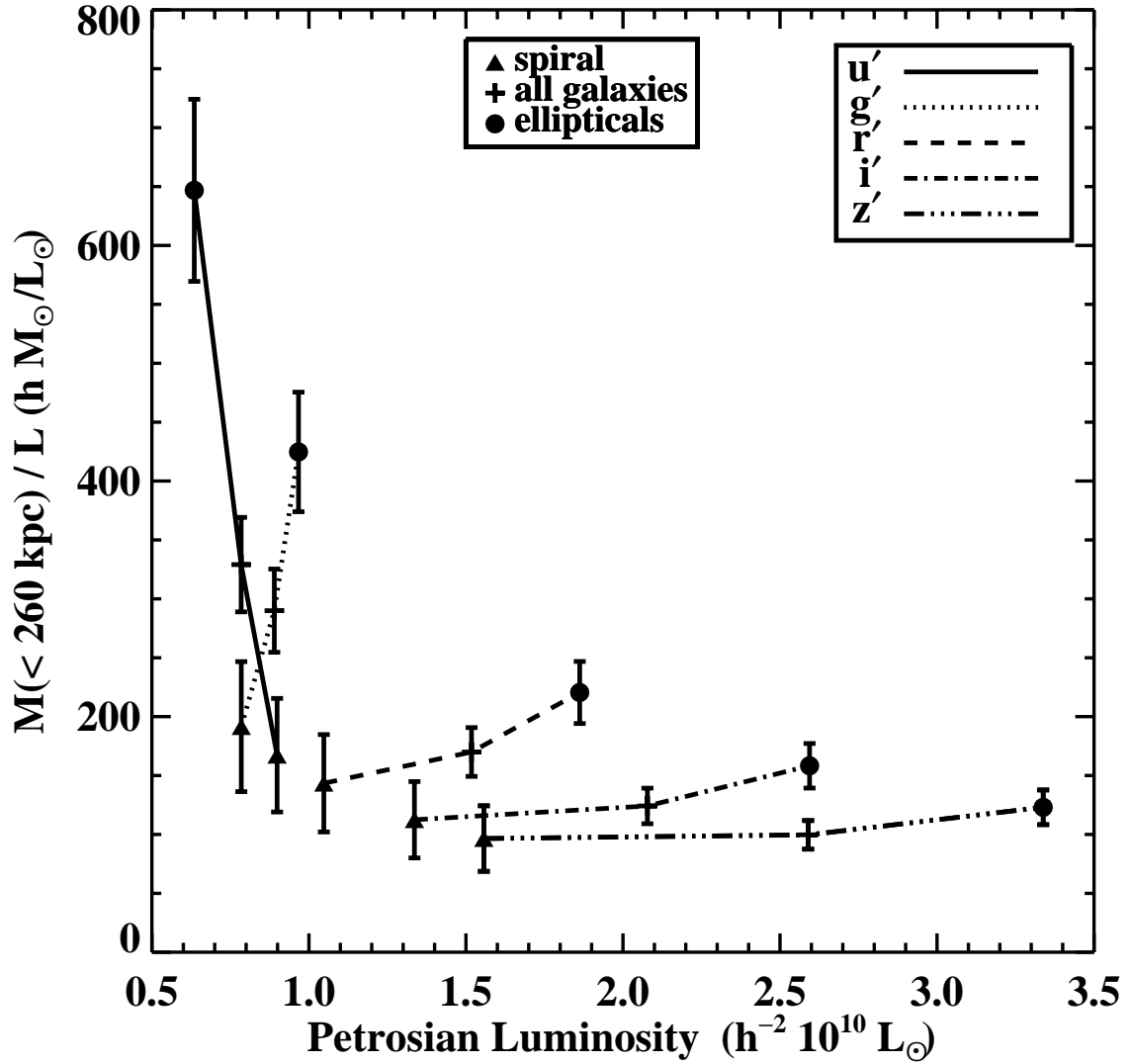
FIG. 19.— This figure shows the mass-to-light ratios $M_{260}/L_{central}$ for various galaxy types in each of the SDSS bands. Filled triangles represent the spiral sample, filled circles the elliptical sample, and plus signs all galaxies. While $M_{260}/L_{central}$ ratios are very type dependent in u' and g', they are essentially type independent in the redder r', i', and z' bands.
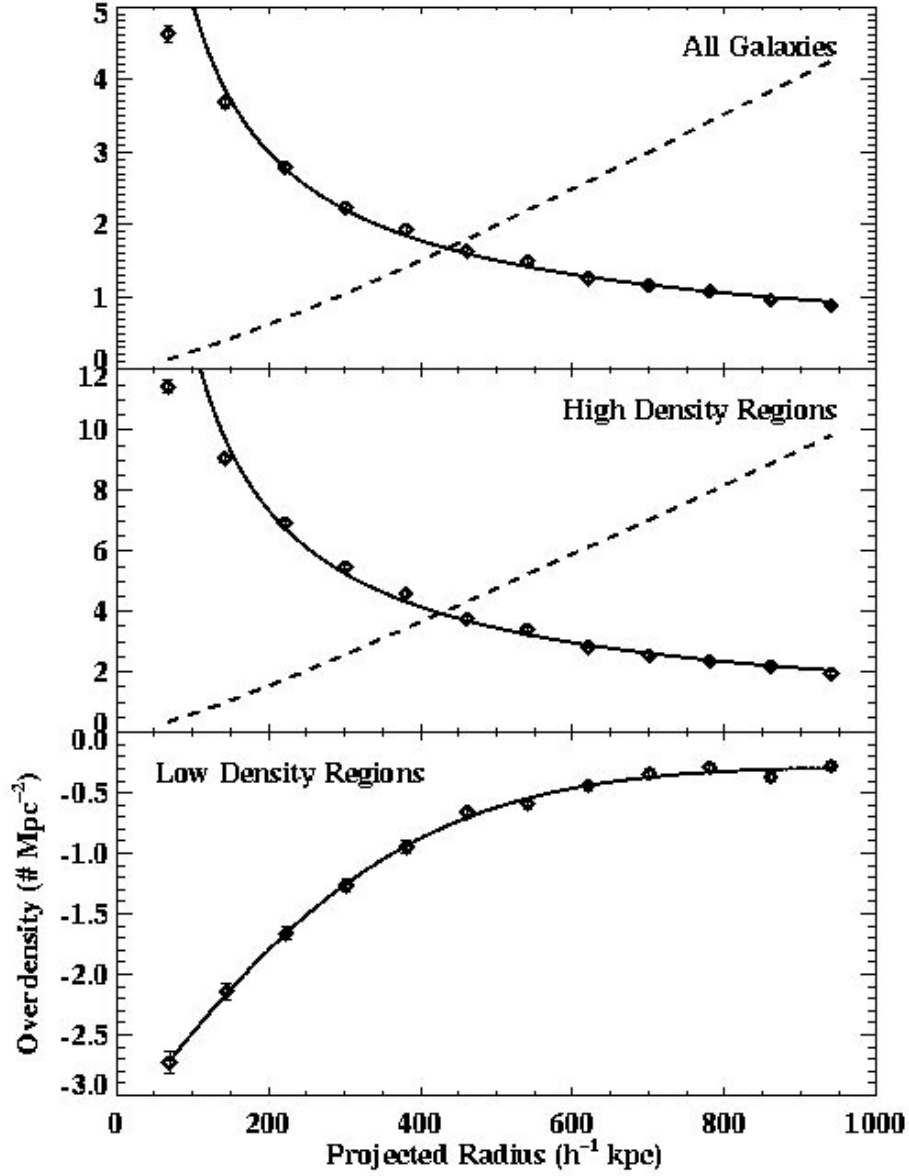
FIG. 20.— Overdensity of bright galaxies around the lens galaxy sample as compared to random points. The overdensity for all lens galaxies, lens galaxies in high density regions and galaxies in low density regions is shown from top to bottom. For the top two plots, the solod line is the best fit power law and the dashed line is the measured cumulative excess number of neighbors. The inner bin deviates from a power law due to undeblended neighbors of the central galaxy. In the bottom plot, the solid line is the best fit negative gaussian.
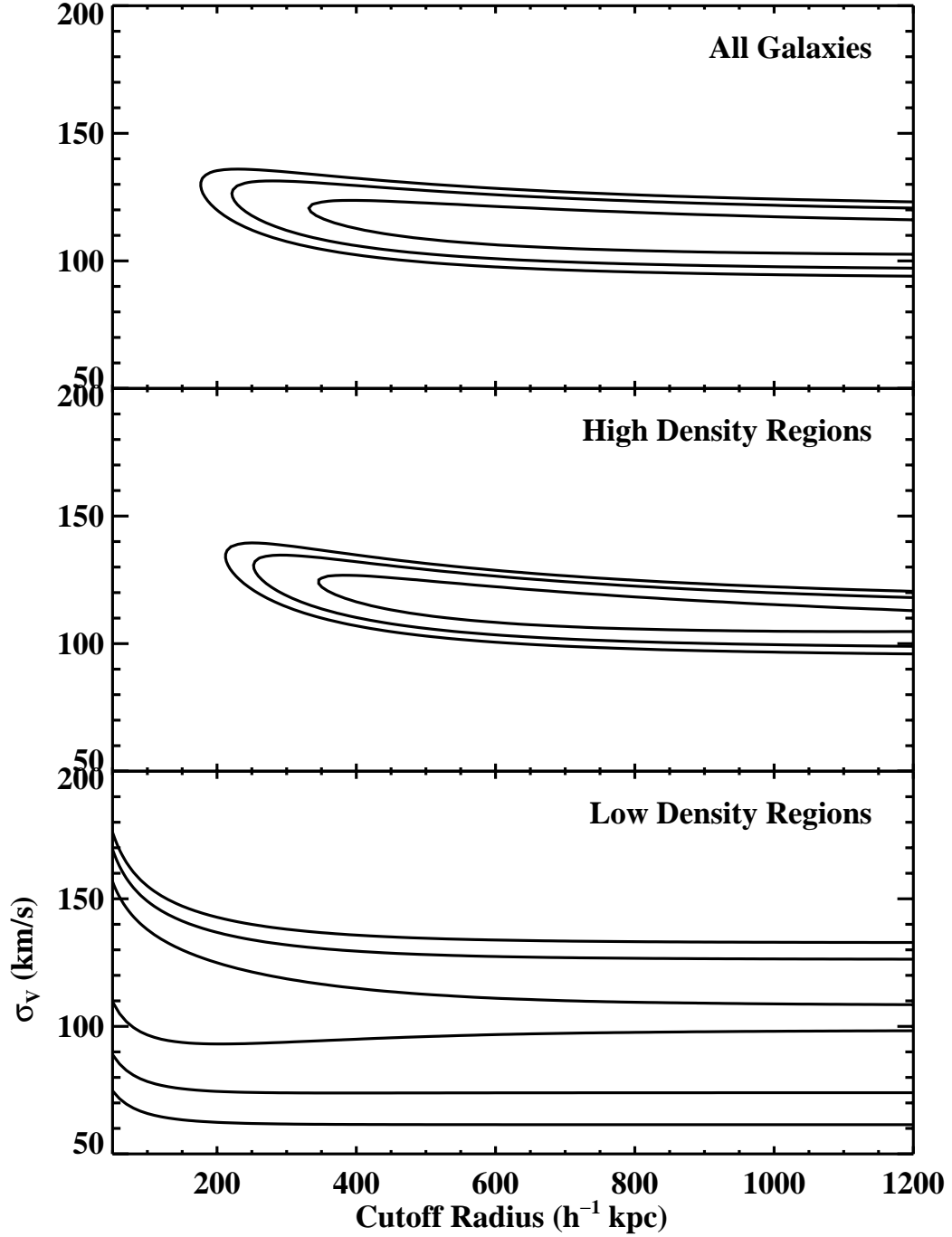
FIG. 21.— χ^2 contours from fits to truncated isothermal spheres for all galaxies, galaxies located in regions of high local galaxy density, and galaxies in regions of low local densiy, shown from top to bottom, respectively. Fits include the contribution to the projected density contrast due to neighboring galaxies. For the average galaxy, the velocity dispersion σ_v is well-constrained, but only a lower bound can be placed on the outer scale. The fits for the low and high density samples is consistent with that of the average galaxy.
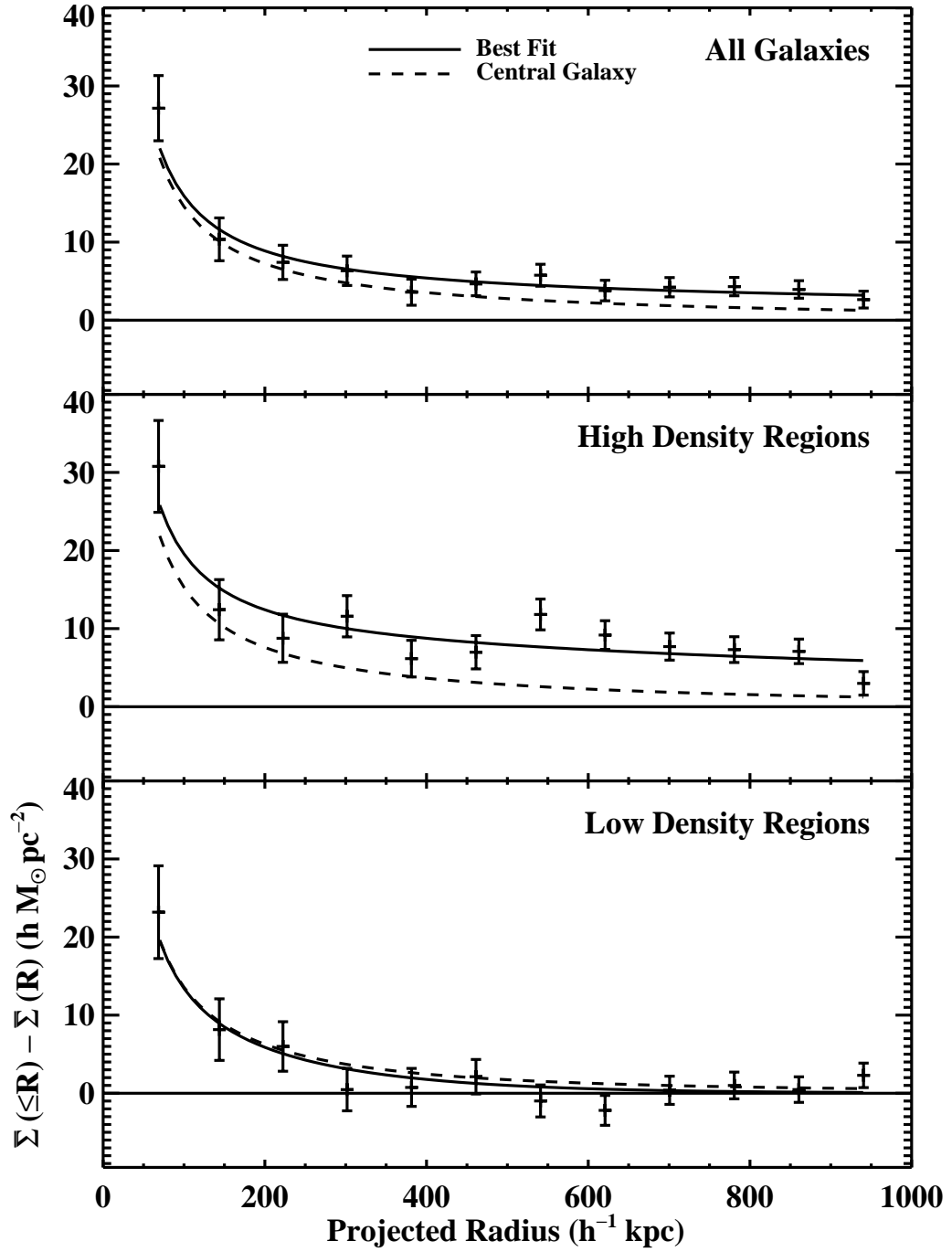
FIG. 22.— Same as figure 7 except this plot shows the combined density contrast for all galaxies, galaxies in high density regions, and galaxies in low density regions, shown from top to bottom, respectively. The solid line is the best-fitting density contrast from a model which includes the central galaxy and neighbors. The dashed line shows only the contribution from the central galaxy. The contribution from neighboring galaxies varies substantially for galaxies in high and low density regions, but the mean central galaxy profile is consistent with that of the average galaxy. This agreement, and the fact that the sub-samples have similar luminosity, suggests that the deconvolution method is accurately accounting for the effects of comparably bright neighbors in the projected density contrast.

TABLE 1
LENSING DATA AND POWER LAW FITS FOR THE GALAXY-MASS CORRELATION FUNCTION

Sample [a]	N_{Lenses} [b]	$\langle\Delta\Sigma_+(20 \leq R \leq 980 \text{ kpc})\rangle$ [c] $\text{h M}_\odot \text{ pc}^{-2}$	A [d] $\text{h M}_\odot \text{ pc}^{-2}$	α [e]
All g'	31039	2.77 ± 0.65	$1.16^{+0.72}_{-0.52}$	$1.19^{+0.26}_{-0.21}$
All r'	31174	4.73 ± 0.51	$3.11^{+0.86}_{-0.78}$	$0.65^{+0.21}_{-0.19}$
All i'	31203	5.70 ± 0.53	$3.63^{+0.86}_{-0.78}$	$0.69^{+0.17}_{-0.16}$
All combined	-	4.59 ± 0.42	$2.55^{+0.68}_{-0.60}$	$0.82^{+0.17}_{-0.16}$
Spirals combined ($g'/r'/i'$)	13806/13882/13904	2.28 ± 0.58	$1.14^{+1.04}_{-0.74}$	$0.88^{+0.57}_{-0.51}$
Ellipticals combined ($g'/r'/i'$)	14097/14156/14157	7.52 ± 0.65	$4.33^{+1.04}_{-0.96}$	$0.81^{+0.15}_{-0.15}$
Low Density Regions ($g'/r'/i'$)	15114/15185/15197	1.18 ± 0.62	$0.25^{+0.53}_{-0.23}$	$1.72^{+0.51}_{-1.06}$
High Density Regions ($g'/r'/i'$)	15568/15631/15642	7.82 ± 0.59	$5.45^{+1.09}_{-1.02}$	$0.56^{+0.17}_{-0.15}$

[a]"All" means all galaxies in the sample. Bandpasses are those in which source galaxy shapes were measured

[b]Number of lenses which passed lensing cuts

[c]$\Delta\Sigma_+ = \Sigma(\leq R) - \Sigma(R)$

[d]Normalization of best-fit power law; $\Delta\Sigma_+ = A(R/1 \text{ Mpc})^{-\alpha}$

[e]Power law index of best-fit power law to GMCF

TABLE 2
LENSING DATA AND MODEL FITS FOR LUMINOSITY BINS

Bandpass [a]	N_{Lenses} [b] $g'/r'/i'$	$\langle L_{Cent} \rangle$ [c] $10^{10} h^{-2} L_\odot$	$\langle \Delta\Sigma_+ (20 \leq R \leq 260\ \text{kpc}) \rangle$ [d] $h\ M_\odot\ \text{pc}^{-2}$	$\langle M(R<260\ \text{kpc}) \rangle$ [e] $10^{12}\ h^{-1}\ M_\odot$	$\langle M(\leq 260\ \text{kpc})/L_{Cent} \rangle$ $h\ M_\odot/L_\odot$
u'	21041/21141/21185	0.494 ± 0.002	7.4 ± 2.5	2.7 ± 0.4	498 ± 66
-	4815/4833/4819	1.342 ± 0.003	15.2 ± 6.1	2.9 ± 0.9	207 ± 64
-	2433/2435/2439	2.133 ± 0.006	11.2 ± 6.7	2.6 ± 1.3	118 ± 62
-	1120/1132/1124	3.76 ± 0.03	23.3 ± 11.4	5.3 ± 2.3	138 ± 59
g'	20960/21061/21096	0.631 ± 0.003	9.2 ± 1.8	2.1 ± 0.4	291 ± 49
-	4910/4933/4928	1.561 ± 0.003	19.5 ± 4.9	4.5 ± 1.0	259 ± 57
-	2440/2439/2434	2.130 ± 0.004	28.8 ± 7.4	6.6 ± 1.5	292 ± 66
-	1110/1120/1120	3.21 ± 0.03	45.9 ± 8.4	10.5 ± 2.2	301 ± 63
r'	20924/21031/21076	0.991 ± 0.005	8.0 ± 1.8	1.8 ± 0.4	166 ± 32
-	4813/4829/4808	3.070 ± 0.007	32.3 ± 5.0	7.4 ± 1.0	228 ± 31
-	2526/2536/2538	4.95 ± 0.02	28.9 ± 8.6	6.6 ± 1.7	126 ± 33
-	1119/1121/1119	8.23 ± 0.06	70.5 ± 18.8	16.1 ± 3.7	187 ± 43
i'	20966/21074/21118	1.298 ± 0.006	7.5 ± 1.8	1.7 ± 0.3	121 ± 25
-	4730/4747/4728	4.28 ± 0.01	36.2 ± 5.0	8.3 ± 1.0	183 ± 22
-	2608/2614/2617	7.35 ± 0.03	29.1 ± 8.6	6.6 ± 1.7	86 ± 22
-	1095/1098/1094	13.7 ± 0.1	90.5 ± 20.4	20.7 ± 4.1	148 ± 29
z'	21036/21148/21191	1.587 ± 0.008	7.7 ± 1.8	1.8 ± 0.3	103 ± 20
-	4711/4723/4706	5.42 ± 0.01	33.2 ± 7.5	7.6 ± 1.0	133 ± 18
-	2579/2586/2587	9.35 ± 0.04	33.4 ± 8.7	7.6 ± 1.7	77 ± 18
-	1091/1094/1091	17.7 ± 0.2	83.2 ± 20.3	19.0 ± 4.0	104 ± 22

[a] Bandpass in which the luminosities were measured

[b] Number of lenses used. Here g', r', and i' refer to the images in which the shapes of source galaxies were measured

[c] Mean luminosity of lens galaxies in this sample and bandpass. Mean luminosities are calculated with the same weights used in the lensing analysis (see §3.4)

[d] Combined density contrast as measured from sources found in g', r', and i' imaging data

[e] Based on fits to singular isothermal spheres

TABLE 3
MASS AND M/L FITS FOR DIFFERENT GALAXY TYPES

Galaxy Type	$\langle M(R{\leq}260\ kpc)\rangle$ [a] $10^{12}\ h^{-1}\ M_{\odot}$	$\langle M/L_{u'}\rangle$ [b] $h\ M_{\odot}/L_{\odot}$	$\langle M/L_{g'}\rangle$ $h\ M_{\odot}/L_{\odot}$	$\langle M/L_{r'}\rangle$ $h\ M_{\odot}/L_{\odot}$	$\langle M/L_{i'}\rangle$ $h\ M_{\odot}/L_{\odot}$	$\langle M/L_{z'}\rangle$ $h\ M_{\odot}/L_{\odot}$
All	2.6 ± 0.3	329 ± 40	290 ± 35	170 ± 21	124 ± 15	100 ± 12
Spirals	1.5 ± 0.4	167 ± 48	192 ± 55	143 ± 41	112 ± 32	97 ± 28
Ellipticals	4.1 ± 0.5	647 ± 77	425 ± 51	221 ± 26	158 ± 19	123 ± 14

[a] Based on fits to singular isothermal spheres

[b] $M = M(R{\leq}260\ kpc)$